# A New Eddy Diffusion Parameterisation for the CSIRO GCM

**Jorgen S. Frederiksen, Martin R. Dix and Antony G. Davies**

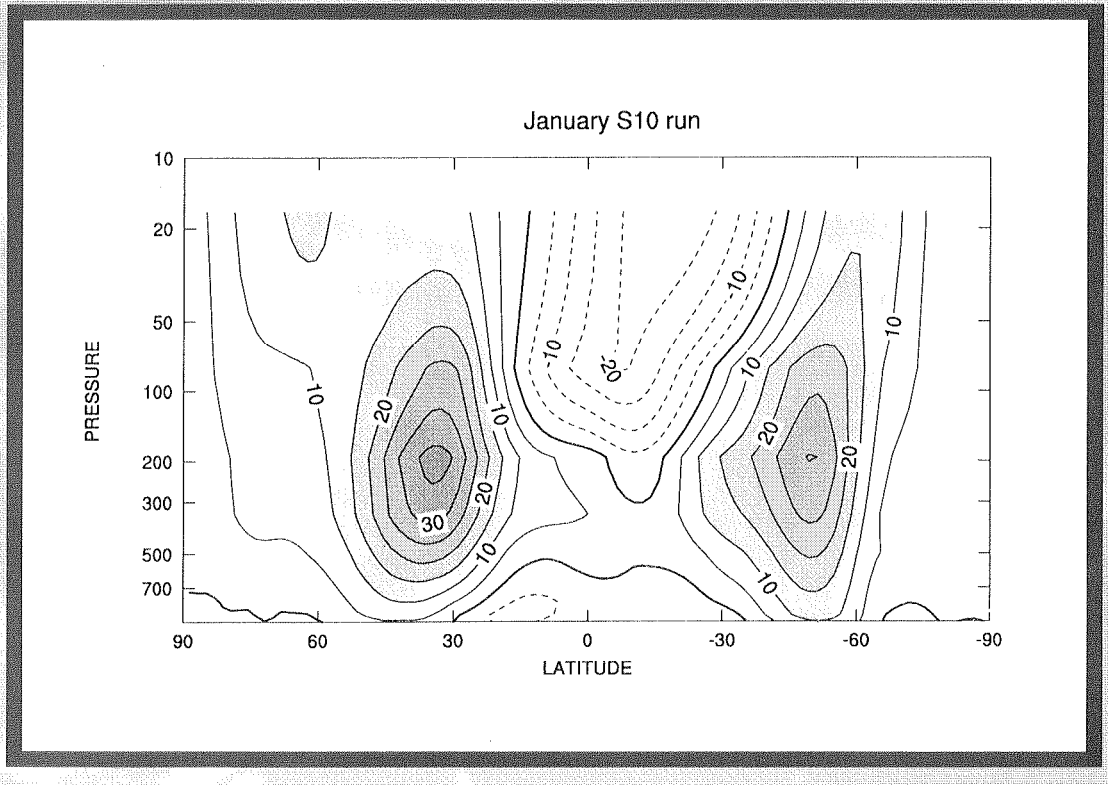


CSIRO

Atmospheric Research

**CSIRO Atmospheric Research Technical Paper No. 44**

# A New Eddy Diffusion Parameterisation for the CSIRO GCM

Jorgen S. Frederiksen, Martin R. Dix and Antony G. Davies

CSIRO Atmospheric Research Technical Paper No. 44

CSIRO Atmospheric Research Technical Papers may be issued out of sequence.

**National Library of Australia Cataloguing–in-Publication Entry**

Frederiksen, Jorgen S.
A New Eddy Diffusion Parameterisation for the CSIRO GCM.

Bibliography.
ISBN 0 643 06499 0.

1. Turbulent diffusion (Meteorology). 2. Atmospheric circulation
I. Dix, Martin R. II. Davies, Antony G.
III. CSIRO. Division of Atmospheric Research. IV. Title. (Series :
CSIRO Atmospheric Research Technical Paper ; no. 44).

551.51

CSIRO Atmospheric Research
PB 1, Aspendale, Victoria 3195, Australia
Ph: (+61 3) 9239 4400; Fax: (+61 3) 9239 4444
E-mail: chief@dar.csiro.au

**Abstract**

A new horizontal eddy diffusion parameterisation based on closure theory has been implemented in the CSIRO Mark II atmospheric global climate model (GCM). Detailed studies of the effects of the parameterisation on the simulated atmospheric circulation, transient kinetic energy and kinetic energy spectra have been carried out for each month of the year. These diagnostics have been compared with corresponding results from observations and from control simulations using an ad hoc diffusion parameterisation also employed in earlier works with this model. The new diffusion parameterisation has improved the simulated atmospheric circulation in the following ways. Zonal and total wave number spectra now have approximate – 3 power laws for ranges of intermediate wave numbers, as in the observations, while the control simulation spectra are considerably flatter. Peak values of transient kinetic energy near the tropospheric jet cores are considerably larger than in the control and in better agreement with observations, particularly in boreal winter. The strength and location of the tropospheric jets are also improved with the new diffusion parameterisation, with monthly averaged zonal mean winds in the NH and SH jet cores stronger than for the control by as much as 5 m s-1 in boreal winter and spring. At T63 resolution, the GCM is stable with a 15-minute timestep with the new eddy diffusion parameterisation, while in the control simulations large amplitude spurious transients are generated throughout the atmosphere over the south polar latitudes if the timestep used exceeds four minutes.

## 1 Introduction

The accuracy of climate simulations, and predictions of weather and climate, by global climate models (GCMs) is strongly dependent on the appropriate treatment of subgrid-scale processes that cannot be explicitly resolved at the finite resolutions of the GCMs. A long standing problem of GCMs has been the significant errors in their simulations of kinetic energy and in its partitioning between eddy and zonal mean kinetic energy. This was a problem with the earliest models of Smagorinsky *et al.* (1965), Manabe *et al.* (1965, 1970, 1979), Miyakoda *et al.* (1971) and Baer and Alyea (1971). To some extent it has also been a problem with more recent models as discussed for example by Hollingsworth *et al.* (1987) and Frederiksen *et al.* (1996). The sensitivity of the large-scale kinetic energy to the strength of the diffusion parameterisation, as found by Manabe *et al.* (1979), was also replicated and studied in more detail by Laursen and Eliasen (1989) and Eliasen and Laursen (1990) who used higher order hyperdiffusion operators to account for the dissipative effects of the unresolved scales.

Frederiksen *et al.* (1996) argued that the parameterisation and strength of the eddy dissipation play major roles in the shape of kinetic energy spectra and in the partitioning between eddy kinetic energy and zonal mean kinetic energy. They examined the resolution dependence of kinetic energy spectra and provided a dynamical explanation for the so-called 'tail-wagging-the-dog' effect where scale-selective dissipation operators cause a drop in the tail of the energy spectra and, surprisingly, also an increase in the large-scale energy. They showed that the cause of this effect relied on the fact that the dissipation operators dissipate enstrophy while leaving the total kinetic energy approximately conserved. A canonical equilibrium model of the effect was presented and it was argued that more soundly based eddy viscosity parameterisations were needed to maintain the correct kinetic energy spectra with changing resolution and to maintain the correct large-scale flow fields.

For the case of two-dimensional turbulence in planar geometry, Leith (1971) calculated a dissipation function that would maintain, as a statistically stationary state, a truncated –3

power law spectrum. He based his formulation on the eddy damped quasi-normal Markovian (EDQNM) closure. Approximations to Leith's dissipation function were used by Boer *et al.* (1984) and Laursen and Eliasen (1989) in their GCM simulations. Frederiksen and Davies (1997) noted that Leith's dissipation function is closely related, but does not correspond exactly to a conventional net eddy dissipation. Koshyk and Boer (1995) obtained a dissipation function similar to Leith's using an empirical method based on ECMWF atmospheric data and employed it in GCM simulations of atmospheric flows and kinetic energy spectra for February.

Frederiksen and Davies (1997) developed eddy drain viscosity, net eddy viscosity and stochastic backscatter parameterisations for barotropic flows on the sphere using eddy-damped quasi-normal Markovian (EDQNM) and direct interaction approximation (DIA) closure models. Their parameterisations, hereafter denoted the FD parameterisations, were shown to be able to maintain essentially the same large-scale kinetic energy spectra with varying horizontal resolution in barotropic model simulations. Frederiksen and Davies also noted the much poorer comparisons between spectra at different resolutions when using a number of different ad hoc eddy viscosity parameterisations.

The purpose of this report is to detail the effect of implementing the net eddy viscosity parameterisation of Frederiksen and Davies (1997) in the CSIRO Mark II GCM. In particular, we compare and contrast the simulated atmospheric circulation and kinetic energy spectra and cross sections, with the FD net eddy viscosity parameterisation, with results employing a control diffusion parameterisation based on a Laplacian dissipation operator that has been used in earlier simulations. The CSIRO Mark II GCM, described in McGregor *et al.* (1993), has been extensively used for climate and climate change simulations (e.g. Dix and Hunt, 1995; Watterson *et al.*, 1995, 1997; Gordon and O'Farrell, 1997; Smith *et al.*, 1997). More recent studies using a triangular T63 resolution, as employed in our current examination, include the works of Smith *et al.* (1998) and Smith (1999).

In section 2, we summarize the formulation of the FD net eddy viscosity parameterisation for barotropic flows on the sphere using EDQNM and DIA closure models. Here we also define a normalized net eddy dissipation function whose functional form will be used in the subsequent sections to define the eddy diffusion. In section 3, we summarize results on the incorporation of the FD net eddy viscosity within a barotropic model. The CSIRO Mark II GCM is briefly described in section 4 including the standard or control formulation of the horizontal diffusion parameterisation. In this section we also examine the simulation of kinetic energy spectra and latitude-pressure cross sections of transient kinetic energy and of monthly averaged and zonally averaged zonal winds for each month of the year. These simulations are compared with corresponding results based on ECMWF data for the years 1985 to 1992 inclusive.

In section 5, we describe the incorporation of the FD net eddy viscosity parameterisation in the CSIRO Mark II model and we compare the simulations with the corresponding results described in section 4 for the control simulation. We examine the sensitivity of our simulations to the strength of the eddy diffusion. Our conclusions are detailed in section 6, focussing on the improvements in the simulations due to the FD net eddy dissipation parameterisation.

## 2 Dynamical subgrid-scale parameterisations

In this section, we briefly summarize the development of eddy viscosity parameterisations for the barotropic vorticity equation following the theoretical and numerical work of Frederiksen and Davies (1997). The barotropic vorticity equation may be written in nondimensional form as

$$\frac{\partial \zeta}{\partial t} = -J(\psi,\zeta) - B\frac{\partial \psi}{\partial \lambda} - D^o + f^o \tag{2.1a}$$

where

$$\zeta = \nabla^2 \psi, \tag{2.1b}$$

$$J(X,Y) = \frac{\partial X}{\partial \lambda}\frac{\partial Y}{\partial \mu} - \frac{\partial X}{\partial \mu}\frac{\partial Y}{\partial \lambda}. \tag{2.1c}$$

Here we have taken $a$ (the earth's radius) and $\Omega^{-1}$ ($\Omega$ is the earth's angular velocity) as length scales and timescales. In Eq. (2.1), $\zeta$ is the vorticity, $\psi$ is the streamfunction, $\mu$ = sin(latitude), $\lambda$ is the longitude, and $t$ the time. Also, $B$ is the beta effect, which with the current scaling would take the value 2 for the atmosphere, although we shall also be interested in the case $B = 0$. The forcing $f^o$ is taken to be Gaussian, spatially isotropic, and temporally white noise forcing, and the representation of the dissipation $D^o$ is given below.

Equation (2.1) may be written in spectral form by expanding each of the functions in spherical harmonics:

$$X(\lambda,\mu,t) = \sum_{m=-T}^{T}\sum_{n=|m|}^{T} X_{mn}(t) P_n^m(\mu) e^{im\lambda}. \tag{2.2}$$

This gives

$$\frac{\partial \zeta_{mn}(t)}{\partial t} = i\sum_p\sum_q\sum_r\sum_s I_{nqs}^{mpr}\zeta_{-pq}(t)\zeta_{-rs}(t) - i\omega_{mn}\zeta_{mn}(t) - D_{mn}^0 + f_{mn}^0. \tag{2.3}$$

Here we write

$$D_{mn}^0 = \nu_0(n)n(n+1)\zeta_{mn}, \tag{2.4}$$

where we refer to $\nu_0(n)$ as the "bare" viscosity. We shall also refer to $f_{mn}^0$ as the "bare" random forcing. In Eq.(2.3),

$$I_{nqs}^{mpr} = -\frac{1}{2}\left(\frac{q(q+1)-s(s+1)}{q(q+1)s(s+1)}\right)K_{nqs}^{m-p-r}, \tag{2.5}$$

$$\omega_{mn} = -\frac{Bm}{n(n+1)}, \tag{2.5b}$$

is the Rossby-wave frequency and

$$K_{nqs}^{mpr} = \int_{-1}^{1} P_n^m \left( pP_q^p \frac{dP_s^r}{d\mu} - rP_s^r \frac{dP_q^p}{d\mu} \right) d\mu, \tag{2.5c}$$

as in Eq.(2.3) of Frederiksen and Sawford (1980). In these equations, $X_{-mn} = X_{mn}^*$ since we take $P_n^{-m}(\mu) = P_n^m(\mu)$ where $P_n^m(\mu)$ are orthonormalized Legendre functions and $X_{mn}$ are spectral amplitudes. Also, $m$ is the zonal wavenumber and $n$ the total wavenumber, while $T$ is the triangular truncation wavenumber, so called because ($m$, $n$) space forms a triangle, as seen from Eq.(2.2). In Eq. (2.3), $p$, $q$, $r$, and $s$ belong to the set $\mathcal{T}$ defined by

$$\begin{aligned}\mathcal{T} = \{p,q,r,s | -T \le p \le T,\ |p| \le q \le T,\\ -T \le r \le T,\ |r| \le s \le T\},\end{aligned} \tag{2.6}$$

Suppose now that the resolution is reduced from triangular truncation $T$ to $T_R < T$, where $T_R$ is the triangular truncation wavenumber of the resolved scales. We define the set $\mathcal{R}$ of resolved scales by

$$\begin{aligned}\mathcal{R} = \{p,q,r,s | -T_R \le p \le T_R,\ |p| \le q \le T_R,\\ -T_R \le r \le T_R,\ |r| \le s \le T_R\},\end{aligned} \tag{2.7}$$

and the set $\mathcal{S}$ of subgrid-scales by

$$\mathcal{S} = \mathcal{T} - \mathcal{R}. \tag{2.8}$$

Thus, for a quadruple ($p$, $q$, $r$, $s$), resolved means that both ($p$, $q$) and ($r$, $s$) are resolved, subgrid means that either ($p$, $q$) or ($r$, $s$) or both are subgrid.

The purpose of a successful subgrid-scale parameterisation is to parameterize the effects of the subgrid-scales so that *statistics* of the resolved scale flow are the same as in the full resolution simulation or in suitable observations. In removing the explicit subgrid-scales information is lost and it is not possible to parameterize the particular phase relationships between resolved scale and subgrid-scale eddies. However, it is possible to successfully parameterize the statistical effects of the subgrid-scale eddies on the resolved scale eddies. Frederiksen and Davies (1997) develop self-consistent subgrid-scale parameterisations based

on EDQNM and DIA closure models. They show that the effects of the subgrid-scale eddies consist of a drain of energy and enstrophy from the resolved scales but that there is also an injection of energy and enstrophy to the resolved scales that is represented by a stochastic backscatter term. This injection may contribute to the growth of instabilities, which may be suppressed in lower-resolution simulations unless a stochastic backscatter term is included (Leith, 1990; Piomelli, *et al.*, 1991). However, most atmospheric circulation models have not accounted for the stochastic backscatter term, but have tried to account for the differences between the drain and injection terms through an effective viscosity.

Frederiksen and Davies (1997) define a (negative) eddy backscatter viscosity $\nu_b$ from the stochastic backscatter term (their Eq.(3.14)) and then define a net eddy viscosity $\nu_n$ as the sum of the eddy drain viscosity $\nu_d$ and the eddy backscatter viscosity $\nu_b$ (their Eq.(3.16)). They show that such a representation of the subgrid-scale eddies works very well when the barotropic model contains reasonable amplitude noise forcing (or if the resolved scale flow is suitably chaotic). The resolved scale flow then satisfies the barotropic vorticity equation

$$\begin{aligned}\frac{\partial \zeta_{mn}}{\partial t} = i\sum_p\sum_q\sum_r\sum_s I^{mpr}_{nqs}\zeta_{-pq}(t)\zeta_{-rs}(t) - i\omega_{mn}\zeta_{mn}(t) \\ -(\nu_o(n)+\nu_n(n))n(n+1)\zeta_{mn}(t) + f^o_{mn}\end{aligned} \tag{2.9}$$

where $p$, $q$, $r$ and $s$ belong to the set $\Re$ and $\nu_n(n)$ is the net eddy viscosity. In this paper, we use net eddy viscosity parameterisations for which $\nu_n(n)n(n+1)$ is proportional to the normalized net eddy dissipation function $g(n/n_*)$, shown in Fig.1a, where $n_* = T$ is the largest retained total wavenumber. Fig.1b shows (in solid) the net eddy viscosity $\nu_n$ for a T31 simulation from Frederiksen and Davies (1997) in which the net eddy dissipation

$$\nu_n(n)n(n+1) = 0.067\, g\left(n/n_*\right) \tag{2.10}$$

and $n_* = 31$. Fig.1b also shows the eddy drain viscosity $\nu_d$ and eddy backscatter viscosity $\nu_b$, which are related to $\nu_n$ through $\nu_n = \nu_d + \nu_b$.

## 3 Net eddy viscosity in the barotropic model

The net eddy viscosity, and eddy drain viscosity and eddy backscatter viscosity, shown in Fig.1b were calculated using EDQNM closure theory. Very similar results are obtained using DIA closure theory as shown in Fig.9b of Frederiksen and Davies (1997). The procedure used to obtain the eddy viscosities was as follows. A barotropic model (with $B = 0$) was used to simulate a typical vertically integrated atmospheric spectrum for January 1979, at resolution T63. The dissipation was taken as a linear combination of a surface drag and a Laplacian dissipation, so that the bare viscosity

$$\nu_o(n) = \begin{cases} \dfrac{1.014\times10^{-2}}{n(n+1)} & \text{for } 2 \le n \le 15 \\ \dfrac{1.014\times10^{-2}}{n(n+1)} + 4.223\times10^{-5} & \text{for } 16 \le n \le 63. \end{cases} \tag{3.1}$$

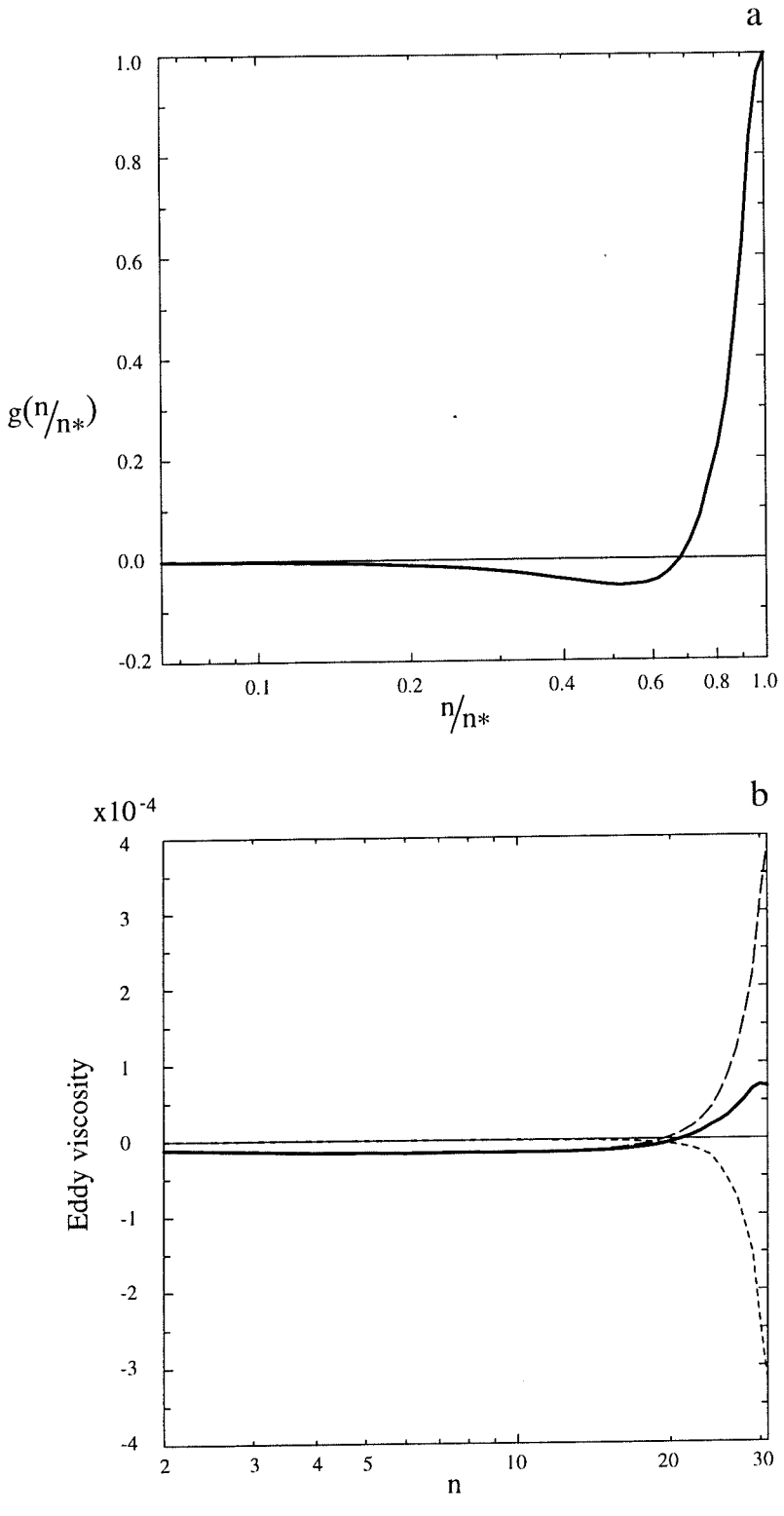


Figure 1 (a) Normalized net eddy dissipation function $g(n/n_*)$ as a function of normalized total wave number $n/n_*$.

(b) Eddy drain viscosity $v_d$ (long dashed), eddy backscatter viscosity $v_b$ (short dashed) and net eddy viscosity $v_n$ (solid) based on a T31 barotropic simulation by FD of the observed January 1979 isotropized kinetic energy spectrum.

The drag contribution ($1.014 \times 10^{-2}$) corresponds to $7.4 \times 10^{-7}$ $s^{-1}$, or an *e*-folding time of 15.6 days, and the Laplacian contribution ($4.223 \times 10^{-5}$) corresponds to $1.25 \times 10^{5}$ $m^2$ $s^{-1}$ in dimensional units.

The EDQNM closure model was then used to calculate the bare random forcing that would exactly maintain the January 1979 spectrum as a statistically stationary state. The January 1979 spectrum was in fact first made isotropic by averaging over zonal wavenumber $m$, so that all components with a given total wavenumber $n$ have the same energy. Observations based on the First GARP (Global Atmospheric Research Program) Global Experiment data were used to construct the spectrum for $n \leq 31$. For larger values of $n$, the spectrum was continued as an $[n(n+1)]^{-3/2}$ spectrum matched to the observations at $n = 31$.

The reason for continuing the observed spectrum as an approximate $n^{-3}$ spectrum is as follows. On the basis of two-dimensional turbulence theory it is expected that the atmospheric spectrum should follow an approximate $n^{-3}$ range at intermediate scales (Kraichnan, 1967, 1971; Leith, 1971). This theoretical result is in reasonably good agreement with spectra calculated on the basis of global observations of the atmosphere (Wiin-Nielsen, 1967, 1972; Boer and Shepherd, 1983). Studies of aircraft data by Nastrom *et al.* (1984) and Nastrom and Gage (1985) indicate an $n^{-3}$ spectrum for scales between approximately 800 and 4000 km and an approximate $n^{-5/3}$ spectral range at smaller scales below about 500 km. However, observational data sets such as the ECMWF data used for generating the January 1979 spectrum in Fig. 2a do not represent the smaller scales sufficiently accurately to establish the power law at smaller scales. This fact has also been noted by Straus and Ditlevsen (1998). In fact, Straus and Ditlevsen find that their observed total wavenumber spectra for winter and summer, based on ECMWF data, are slightly shallower than $n^{-3}$ between wavenumbers 15 to 35 and then fall off more steeply for higher wavenumbers.

A 150 day direct numerical simulation (DNS) of the barotropic model at T63 and with the above bare viscosity and bare random forcing was then performed. Averages over the last 100 days of the simulation were used to create the kinetic energy spectrum $e(n)$ (long dashed) and standard deviation $\sigma(n)$ (short dashed) shown in Fig.2. Here $e(n)$ is the sum over the zonal wavenumbers of the kinetic energy in components $(m,n)$ and $\sigma(n)$ is the corresponding standard deviation over 100 days. Fig.2a also shows the total wavenumber spectrum for the January 1979 observed spectrum (thin solid). As is evident, there is generally good agreement between the T63 simulation, which is taken as the 'truth' or standard simulation, and the January 1979 observed spectrum.

The EDQNM closure theory was then used to calculate the eddy viscosities that would maintain approximately the same large-scale spectra when the resolution is reduced to T31 (or T15). Fig.2a also shows the results (scaled by $10^{-1}$) of large eddy simulations (LES) with the appropriate net eddy viscosity at T31 and for $B = 0$ (thick solid). Also shown in Fig.2a, scaled by $10^{-1}$, are January 1979 (thin solid) and DNS (long dashed) results calculated at T63, but reduced to T31 for comparison with LES at T31. Fig.2b shows similar results for $B = 2$, that is, with rotation, at T63 and T31 and using a net eddy viscosity parameterisation at T31.

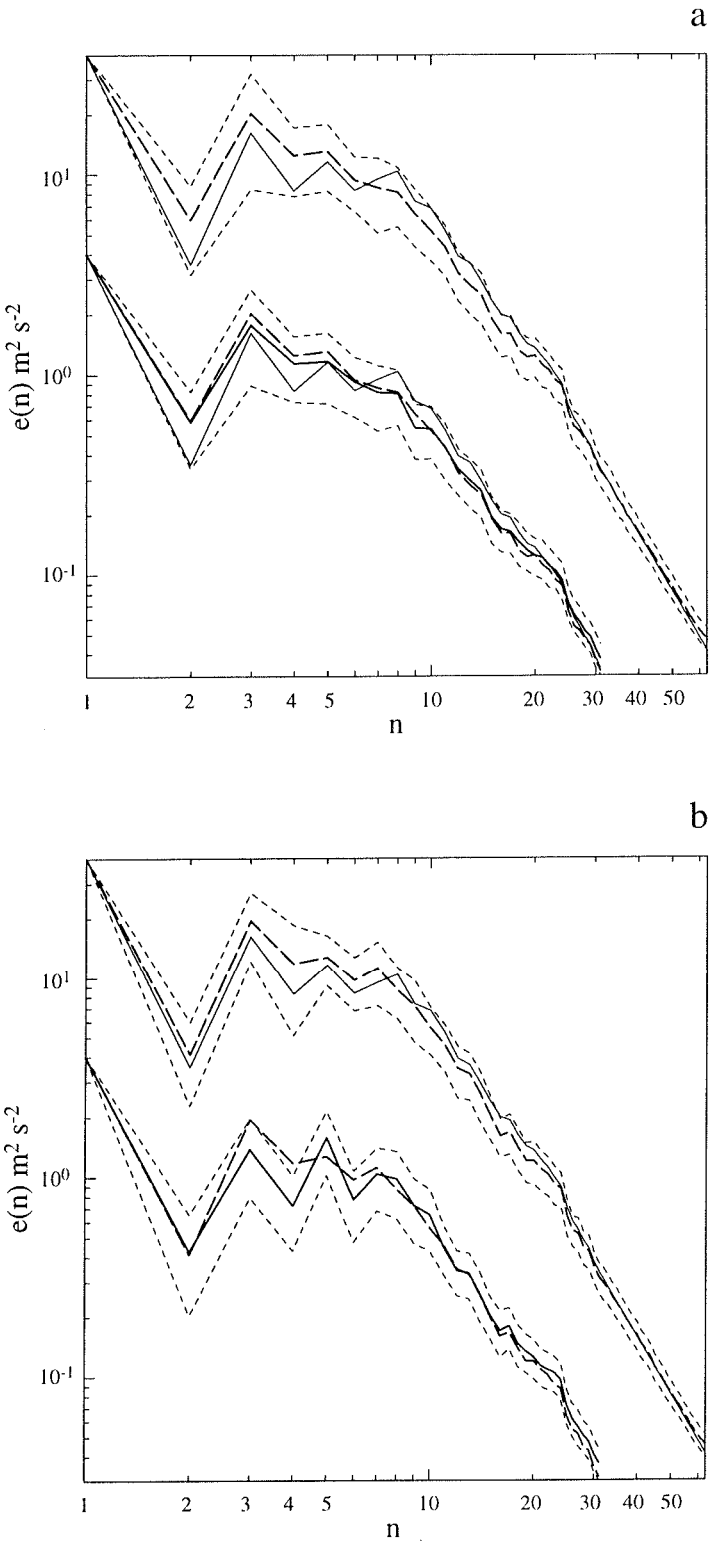


Figure 2 (a) Kinetic energy spectra $e(n)$ ($m^2s^{-2}$) for isotropized January 1979 (thin solid), DNS at T63 (long dashed), LES at T31 (thick solid) and $e(n) \pm \sigma(n)$ (short dashed) for DNS or LES. The results are for $B = 0$ with T31 LES scaled by $10^{-1}$. Also shown, scaled by $10^{-1}$, are January 1979 and DNS results calculated at T63 but reduced to T31 for display.

(b) As in Fig.2a but for $B = 2$.

We see from Figs 2a and b that the EDQNM derived eddy viscosities yield total wavenumber spectra for which there is generally good agreement between the T63 DNS and T31 LES at the smaller scales with some deviations at the larger scales. The latter may be due to the very long eddy turn over times of these components and the few *m* values that are averaged over at the large-scale end of the system.

The normalized dissipation function $g(\eta/\eta_*)$ shown in Fig.1a has been obtained from the T31 eddy viscosity, used in Figs 2a and b, through the relationship (2.10).

## 4 GCM simulations with standard diffusion

The CSIRO atmospheric GCM, that we use for the simulations described in this section and in section 5, is described in detail by McGregor *et al.* (1993). Briefly the CSIRO Mark II model is a 9-level general circulation model that simulates the primitive equations of motion of the global atmosphere. It incorporates a comprehensive array of physical processes that force the dynamical and thermodynamic equations. It incorporates diurnal and seasonal cycles of forcing. It includes radiation and precipitation, and major properties such as snow, sea-ice and cloud amount are determined self-consistently. The model includes an interactive land surface scheme but sea-surface temperatures are prescribed in the version used for the present study and are interpolated in time from the monthly fields of the Bottomley *et al.* (1990) climatology for 1951-1980. Vertical diffusion in the model is parameterized in terms of a stability-dependent K theory following Blackadar (1962). The model uses the flux form of the dynamical equations.

The model uses the sigma coordinate in the vertical where $\sigma = p/p_s$ with $p$ the pressure and $p_s$ the surface pressure. The main prognostic variables are the surface pressure $p_s$, and the surface pressure weighted vorticity, $\hat{\zeta} = p_s\zeta$, divergence, $\hat{D} = p_s D$, temperature $\hat{T} = p_s T$ and moisture mixing ratio $\hat{q} = p_s q$ at all nine levels. These variables are carried as spherical harmonic coefficients or spectral fields except for the moisture mixing ratio, which is carried on a Gaussian grid. The current version of the model uses the sigma levels

(0.9793, 0.9136, 0.8032, 0.6598, 0.5000, 0.3401, 0.1968, 0.0864, 0.0208)

for calculation of the main prognostic variables. It also uses a horizontal resolution corresponding to triangular truncation T63. It uses a semi-implicit leap frog timestepping scheme together with an Asselin time filter. The timestep used in these simulations varies between 4 and 15 minutes.

### 4.1 Standard horizontal diffusion parameterisation

Horizontal diffusion is applied to the surface pressure weighted vorticity $\hat{\zeta}$, divergence $\hat{D}$ and temperature fields $\hat{T}$. It is not applied to the surface pressure or to the moisture mixing ratio, which is treated using a semi-Lagrangian advection scheme that is slightly diffusive (McGregor, 1993). Let $\hat{\zeta}_{mn}$, $\hat{D}_{mn}$ and $\hat{T}_{mn}$ represent the dimensional spectral coefficients of $\hat{\zeta}$, $\hat{D}$ and $\hat{T}$ respectively. Then the standard diffusion parameterisations for vorticity, divergence and temperature have the forms

$$\frac{\partial \hat{\zeta}_{mn}}{\partial t} \sim -\frac{K_\zeta^d}{a^2}\Delta(n)n(n+1)\hat{\zeta}_{mn} \tag{4.1a}$$

$$\frac{\partial \hat{D}_{mn}}{\partial t} \sim -\frac{K_D^d}{a^2}\Delta(n)n(n+1)\hat{D}_{mn} \tag{4.1b}$$

$$\frac{\partial \hat{T}_{mn}}{\partial t} \sim -\frac{K_T^d}{a^2}\Delta(n)n(n+1)\left\{\hat{T}_{mn} - \left(\overline{T} + \sigma\frac{\partial \overline{T}}{\partial \sigma} - T_o\right)p_{smn}\right\} \tag{4.1c}$$

Here $\overline{T}$ is the global mean $\sigma$-level temperature and $T_o$ is an isothermal temperature taken as 290K. The function $\Delta(n)$ is a cut-off function, which restricts the dissipation to the small scales; the standard diffusion parameterisation at T63 uses

$$\Delta(n) = \begin{cases} 1 & 60 \le n \le 63 \\ 0 & \text{otherwise} \end{cases} \tag{4.2}$$

resulting in a very scale selective dissipation operator. The standard diffusion parameterisation also uses the dimensional vorticity diffusion coefficient $K_\zeta^d = 6.25\times10^4\,\mathrm{m^2 s^{-1}}$ corresponding to a nondimensional coefficient of $K_\zeta = 2.112\times10^{-5}$. It also sets $K_T^d = K_\zeta^d$ and $K_D^d = 4K_\zeta^d$; the larger diffusion coefficient for divergence was chosen to ensure numerical stability in the stratosphere for reasonably large time steps (H.B. Gordon, 1999; personal communication).

After an initial spin up, in which the CSIRO GCM reached its climatological state, the model was further integrated in the control mode for 10 years. This 10-year data set was then used to generate the kinetic energy spectra, kinetic energy cross sections and mean zonal wind cross sections described in the following subsections.

## 4.2 Kinetic energy spectra for control simulation

Next, we examine the kinetic energy spectra for the control simulation focussing on the results for January for comparison with the barotropic results of section 3 and the observed spectra for January 1979. Figs 3a and 3b show, respectively, the mean and mean ± standard deviation of the dimensional total wave number kinetic energy spectrum $e(n)$ and zonal wave number kinetic energy spectrum $E(m)$ in $m^2\ s^{-2}$ for January for the control GCM simulation. Here the kinetic energy spectra include both the rotational and divergent components of the wind and are averages over the model levels and the 10 simulated Januaries. We see from Fig. 3a that the control simulation underestimates the kinetic energy at total wave numbers between 5 and 25 compared with the observed spectra for January 1979. At small scales the kinetic energy is too large compared with the observations continued as an $[n(n+1)]^{-3/2}$ spectrum matched to observations at $n = 31$. The zonal wavenumber spectrum $E(m)$ shown in Fig. 3b is again flatter than observed (Wiin-Nielsen, 1967, 1972; Leith, 1971), being closer to an $m^{-2}$ spectrum than to an $m^{-3}$ spectrum between $m \approx 7$ to 40.

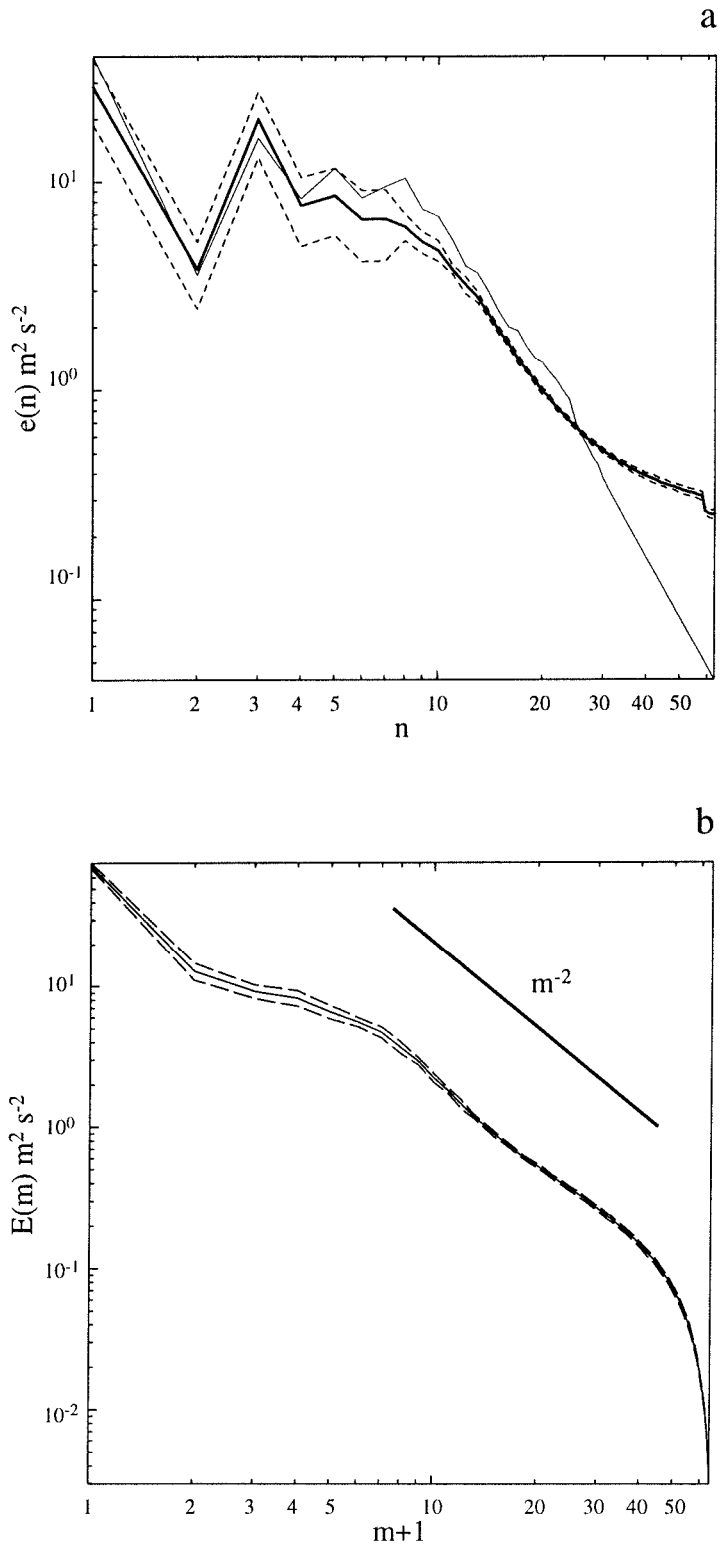


Figure 3 (a) Kinetic energy spectra $e(n)$ ($m^2 s^{-2}$) for isotropized January 1979 (thin solid), control GCM simulation for January (thick solid), $e(n) \pm \sigma(n)$ (dashed) for control simulation for January.

(b) Kinetic energy spectra $E(m)$ ($m^2 s^{-2}$) for January control simulation (solid) and $E(m) \pm \Sigma(m)$ (dashed), where $\Sigma(m)$ denotes the standard deviation.

From the modelling studies on the effects of the strength of the diffusion on spectra and circulation reviewed in the Introduction, it is expected that the too flat control spectrum at small scales and the too low energy at intermediate scales is symptomatic of the tail-wagging-the-dog effect. That is, the scale selective dissipation is too weak resulting in an increase of kinetic energy at small scales and, for the reasons outlined by Frederiksen *et al.* (1996), a decrease in kinetic energy at intermediate and some large-scales. As noted by Frederiksen *et al.*, the counter intuitive behaviour at intermediate and large-scales is due to the fact that scale selective diffusion operators dissipate enstrophy but have less effect on the energy. Thus decreasing the scale selective dissipation will tend to increase the enstrophy to energy ratio and result in a flat spectrum, while increasing the dissipation will decrease this ratio and send excess energy to larger scales and result in a steeper spectrum. We also notice from Fig. 3a that there is a distinct drop in the kinetic energy spectrum at wavenumbers 60 to 63. This is a reflection of the fact that the scale selection operator $\Delta(n)$ in Eq. (4. 2) for the control run is too scale selective. It attempts to confine the dissipation range to the wavenumbers $n \approx 60$ to 63.

### 4.3 Transient kinetic energy cross sections

Many models of the atmospheric general circulation tend to have too little transient kinetic energy, as reviewed in the Introduction. This is also the case with the control CSIRO Mark II model as shown in Fig. 4. Fig. 4a shows cross sections of zonally averaged transient kinetic energy based on twice daily January ECMWF data for the years 1985 to 1992, while Fig. 4b shows the corresponding cross sections for the control simulation based on twice daily data for January for 10 years of integration. We note the significantly smaller peak amplitudes in both the Northern and Southern Hemispheres in the control simulation compared with the observations. For example, in the Northern Hemisphere the peak transient kinetic energy is 187 $m^2s^{-2}$ in the control compared with 220 $m^2s^{-2}$ at 300 mb near 50°N and 231 $m^2s^{-2}$ at 250 mb near 40°N in the observations, and in the Southern Hemisphere it is 144 $m^2s^{-2}$ in the control compared with 219 $m^2s^{-2}$ in the observations.

The results in Fig.4b have been obtained using a 4 minute timestep in the simulations. Increasing the timestep above this to, say, 15 minutes, which is commonly used with a T63 resolution, results in large amplitude spurious transients throughout the atmosphere over the south polar latitudes. In section 5, we note that these spurious transients result from inadequacies in the standard diffusion parameterisation with the larger timestep.

### 4.4 Mean zonal winds

Next we compare the control zonal mean wind cross sections based on 10 years of simulation with ECMWF data for the period 1985 to 1992. These have been calculated for each month but we shall focus here on the averages for January, April, July and October. Fig. 5 shows the mean zonal winds for the observations and control simulations in these months. For January we note that while the main features of the circulation are simulated, both the Northern and Southern Hemisphere jetstream maxima are underestimated and the Northern Hemisphere stratospheric jet is too weak. In these respects, the current T63 control simulation is similar to the rhomboidal R21 control simulation of McGregor *et al.* (1993, Fig.8a) for December-January-February. Between January and April the strength of the NH tropospheric jet decreases in the observations and, by a larger factor, in the control simulations. The resultant

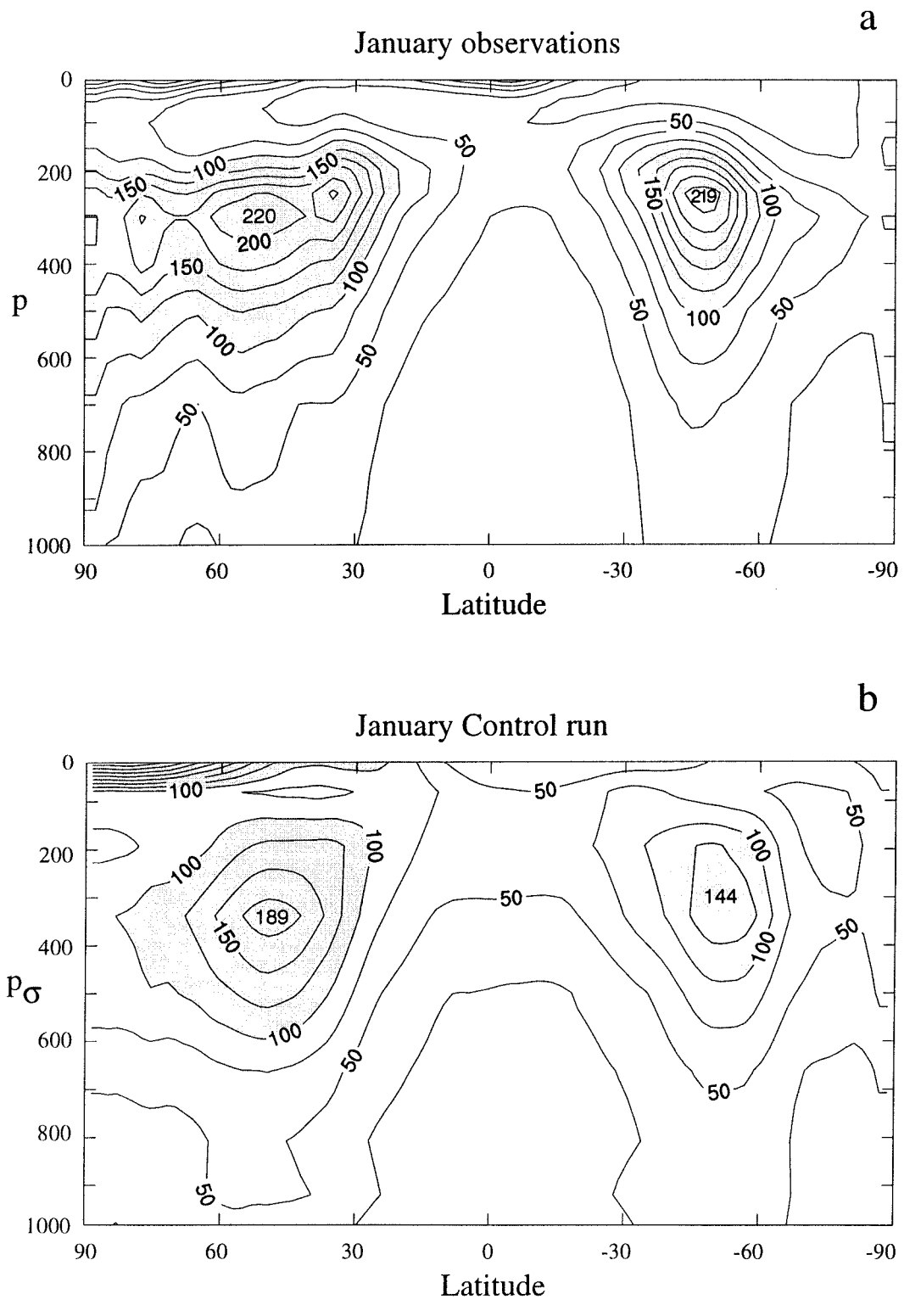


Figure 4 (a) Monthly and zonally averaged transient kinetic energy cross sections as functions of latitude and pressure $p$ for January ECMWF observations for 1985 to 1992.

(b) As in Fig.4a for control simulations as functions of latitude and $p_\sigma = 1000\sigma$.

jetstream maximum in the control run in April is about 8 m $s^{-1}$ weaker than in the observations. In both January and April, and in the intervening months, the NH tropospheric jetstream maxima also tend to be displaced poleward in comparison with the observations. In general, comparison between observations and the control run tends to be better in the SH during this period, although in the control simulation the SH stratospheric jet is somewhat too strong.

Between April and July, the NH tropospheric jet decreases in strength in the observations and to a greater extent in the control simulation with the deficit being close to 12 m $s^{-1}$ in the jet core in July. The SH simulation is again better with the tropospheric jet only about 5 m $s^{-1}$ too weak in July and the stratospheric jet close to observations.

During the second half of the year the NH circulation increases in strength and the comparison between the observations and the control run improves as also shown in Fig.5 for October. For this month, the NH tropospheric jet cores for the observations and the control simulations are closely comparable in both their strengths and locations. The separation of stratospheric jet in the NH is evident in the observations in October but not in the control run. In fact the control run also underestimates the strength of the NH stratospheric jet throughout the boreal winter season. In the SH, the control simulation of the jet structure is quite good both in the troposphere and stratosphere, although the maximum strength of the tropospheric jet in October is about 5 m $s^{-1}$ too weak compared with the observations. In November and December (not shown), the NH tropospheric circulation strengthens and the SH circulation weakens in both the observations and the control run. As is the case for January however, the NH tropospheric jet in the control has peak values that are underestimated by between 5 and 8 m $s^{-1}$.

In many respects the control simulations at T63 horizontal resolution are quite similar to the R21 simulations described by McGregor *et al.* (1993) and Watterson *et al.* (1995). This reflects the very similar physical parameterisations used in the two versions of the model. McGregor *et al.* give details of other circulation properties of the control simulations of the CSIRO model. These include zonal means of the meridional winds and temperatures, as functions of latitude and pressure, and latitude-longitude plots of sea-level pressure and 500 mb zonal winds. The current T63 control simulations of these fields are broadly similar to the R21 results of McGregor *et al.* and will not be displayed here as our interest is primarily in the mean zonal winds (and kinetic energies).

## 5 GCM simulations with net eddy viscosity parameterisation

### 5.1 Net eddy viscosity parameterisation

In this section we parameterize the form of the horizontal diffusion in terms of the normalized net dissipation function $g(n/n_*)$ of Fig. 1 where $n_* = 63$ for our T63 simulations; vertical diffusion is parameterized as described in section 4. If our dissipation function had been derived on the basis of spectra having an infinitely long $n^{-3}$ enstrophy cascading inertial range then we would expect that it would satisfy a scaling relationship with varying resolution (Leith, 1971; Frederiksen and Davies, 1997). That is, the dissipation would have the universal form $g(n/n_*)$ for varying resolution $n_*$ but the strength of the dissipation required to maintain the $n^{-3}$ inertial range as a statistically stationary state would depend on

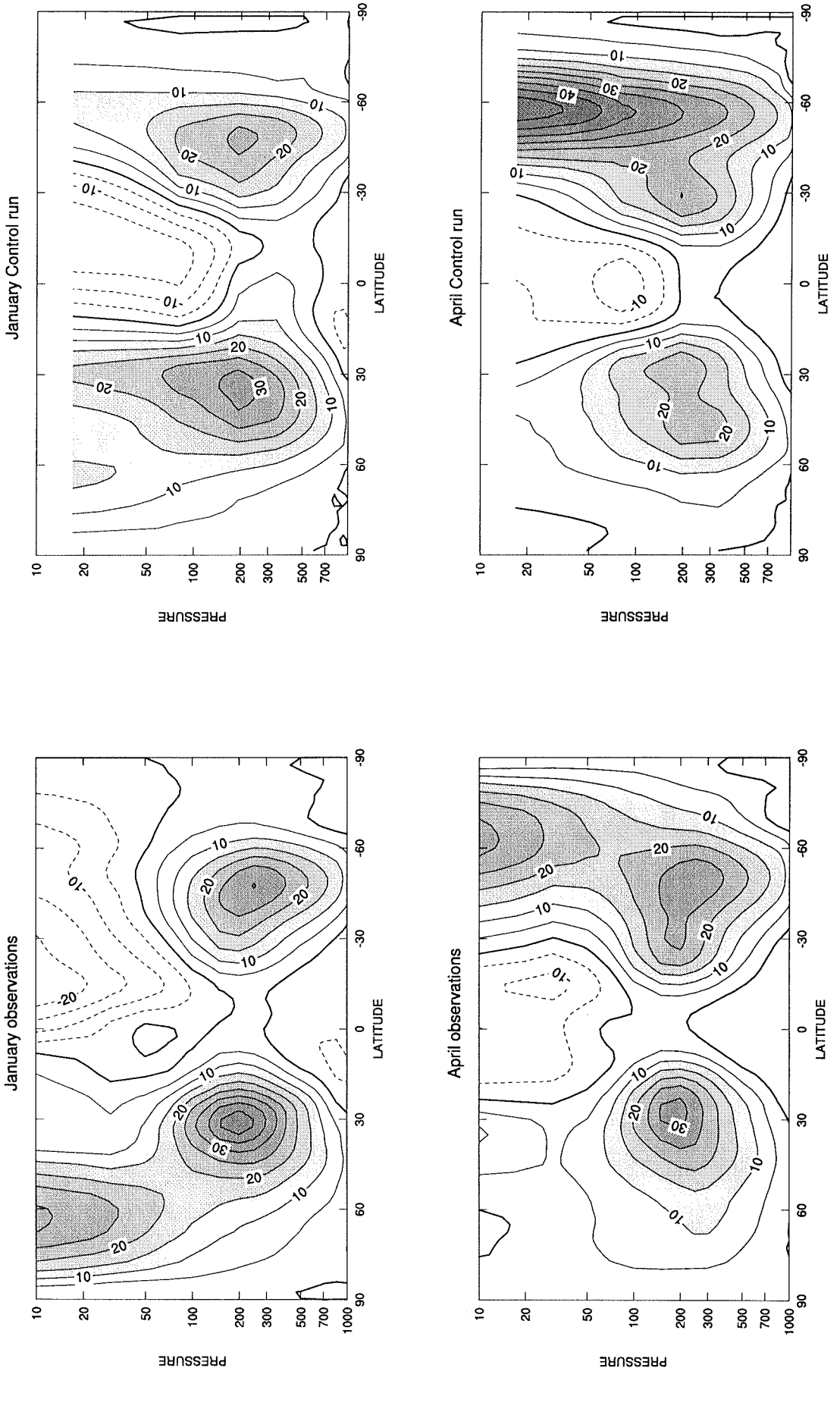


Figure 5 Monthly and zonally averaged zonal wind cross sections as functions of latitude and pressure based on ECMWF observations for 1985 to 1992 and for control simulations.

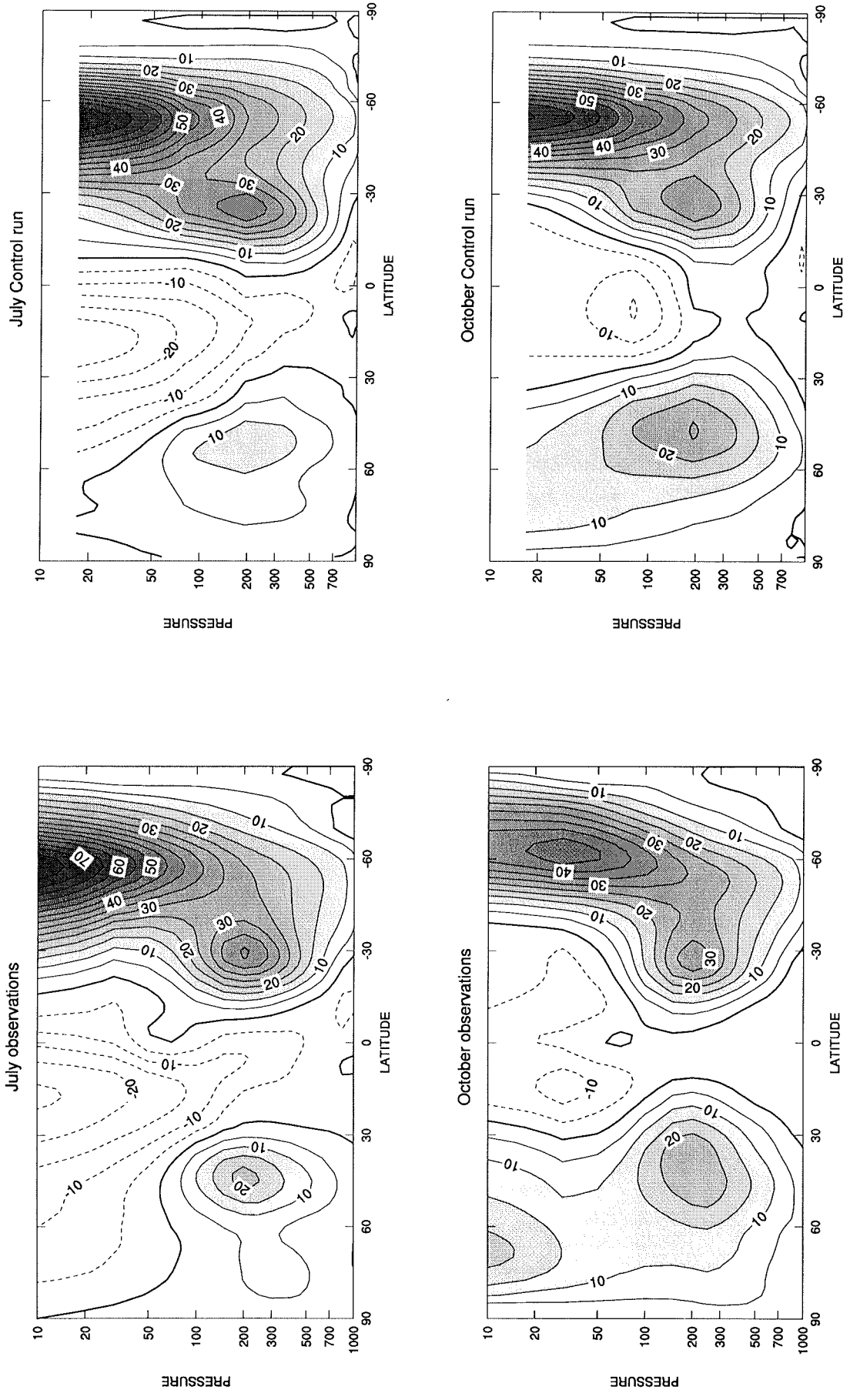


Figure 5 (cont) Monthly and zonally averaged zonal wind cross sections as functions of latitude and pressure based on ECMWF observations for 1985 to 1992 and for control simulations.

the resolution. Our spectra differ from this idealized form; in particular, they are more complicated at small wavenumbers and as a consequence we do not expect exact universality for our net dissipation function. However, we expect it to be approximately universal. Indeed, comparison of the net eddy viscosity of Frederiksen and Davies (1997, Figs. 3c and 4) at T31 and T15 indicates such an approximate universality even at these rather low resolutions.

The new diffusion parameterisations then take the forms

$$\frac{\partial \hat{\zeta}_{mn}}{\partial t} \sim -S[0.067\Omega] g\left(n/n_*\right) \hat{\zeta}_{mn} \sim -S \frac{\tilde{K}_\zeta^d}{a^2} \left[g\left(n/n_*\right) n_*(n_*+1)\right] \hat{\zeta}_{mn} \tag{5.1a}$$

$$\frac{\partial \hat{D}_{mn}}{\partial t} \sim -S \frac{\tilde{K}_D^d}{a^2} \left[g\left(n/n_*\right) n_*(n_*+1)\right] \hat{D}_{mn} \tag{5.1b}$$

$$\frac{\partial \hat{T}_{mn}}{\partial t} \sim -S \frac{\tilde{K}_T^d}{a^2} \left[g\left(n/n_*\right) n_*(n_*+1)\right] \left\{ \hat{T}_{mn} - \left( \overline{T} + \sigma \frac{\partial \overline{T}}{\partial \sigma} - T_o \right) p_{smn} \right\} \tag{5.1c}$$

where $\tilde{K}_\zeta^d = \dfrac{0.067 a^2 \Omega}{n_*(n_*+1)} = 4.92 \times 10^4 \, \mathrm{m^2 s^{-1}}$ since $n_* = 63$. The dimensional vorticity diffusion coefficient $\tilde{K}_\zeta^d$ corresponds to a nondimensional diffusion coefficient of $\tilde{K}_\zeta = 1.662 \times 10^{-5}$. These diffusion coefficients are only slightly smaller than the corresponding coefficients for the standard diffusion parameterisation used in section 4. As in section 4, we take $\tilde{K}_T^d = \tilde{K}_\zeta^d$ and $\tilde{K}_D^d = 4\tilde{K}_\zeta^d$. We note that with the scaling factor $S$ set to unity then Eqs (5.1a) to (5.1c) have the same form as Eqs (4.1a) to (4.1c) respectively but with the replacement

$$\Delta(n) n(n+1) \rightarrow g\left(n/n_*\right) n_*(n_*+1) . \tag{5.2}$$

Note that both these functions have the value $n_*(n_*+1)$ at $n = n_*$.

In Eq. (5.1) a scaling factor of $S$ = 1 would be appropriate for the barotropic model at resolution T31 and for the vertically averaged flows considered in sections 2 and 3. For the T63 GCM a larger $S$ would be appropriate, which could also depend on the sigma level (Koshyk and Boer, 1995). However, here we shall follow the approach of the standard dissipation parameterisation and many other GCMs and choose a single value for $S$. We assume similar diffusion processes for the vorticity, divergence and temperature equations as shown in Eqs. (5. 1a) to (5. 1c) and examine the sensitivity of the circulation to the magnitude of $S$. We also note that most GCMs use parameterisations for which the dissipation is purely non-negative at every wavenumber while $g\left(n/n_*\right)$ is in fact weakly negative for intermediate wave numbers with a positive cusp at large wavenumbers. The dissipation averaged over wavenumbers is of course positive. We shall also perform simulations in which only the positive contribution to $g\left(n/n_*\right)$ is included. We define

$$g^{+}\left(n/n_{*}\right)=\begin{cases} g\left(n/n_{*}\right) & \text{if } g \geq 0 \\ 0 & \text{otherwise.} \end{cases} \tag{5.3}$$

In the following subsections we describe the results of a number of simulations using the dissipation functions $g^{+}\left(n/n_{*}\right)$ and $g\left(n/n_{*}\right)$. We consider simulations for which $S = 1$, 5, 10 and the dissipation function is $g^{+}\left(n/n_{*}\right)$, denoted runs $S1$, $S5$ and $S10$ respectively, and a simulation for which $S = 5$ and the dissipation function is $g\left(n/n_{*}\right)$, denoted run $N5$. The results presented in the following subsections are based on 10 years of model data to generate the monthly averages.

## 5.2 Kinetic energy spectra

Fig. 6 shows the mean dimensional total wave number kinetic energy spectrum $e(n)$ in $m^2 s^{-2}$ for January for the $S1$, $S5$, $S10$ and $N5$ simulations and as well the January 1979 spectrum is shown for comparison. The results are based on averages over 10 Januaries. We see that the energy spectra for $S5$ and $S10$ follow the observed spectra quite well at most scales, with the main differences between S5 and S10 occurring at the very small scales. The $N5$ spectrum also closely follows the observed spectrum at wavenumbers smaller than about 25 but for larger wavenumbers there is some overestimation of the energy compared with the continued $n^{-3}$ spectum.

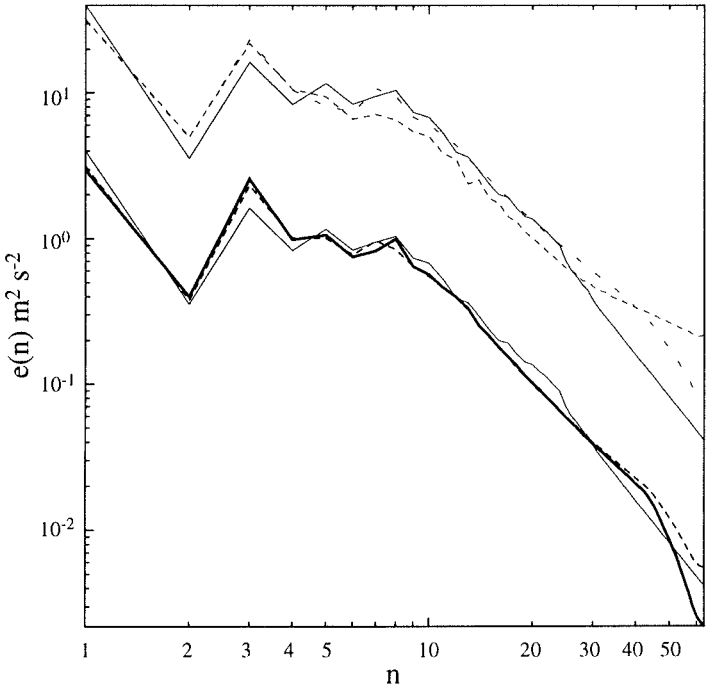


Figure 6 Kinetic energy spectra $e(n)$ $(m^2 s^{-2})$ for January 1979 (thin solid), S1 run (thin short dashed), N5 run (thin long dashed), S5 run (x $10^{-1}$) (thick short dashed) and $S10$ run (× $10^{-1}$) (thick solid) where the simulations are all for January.

The close correspondences between the *S*5, *S*10 and January 1979 spectra contrast with the *S*1 spectrum, which underestimates the kinetic energy at total wave numbers between 5 and 25 compared with the observed spectra. As well, the *S*1 spectrum has too large a kinetic energy at small scales compared with the approximately $n^{-3}$ continuation of the observed January spectrum. In these respects the *S*1 spectrum is similar to the control simulation spectrum in Fig. 3a (however, it does not have the sudden drop in the spectrum at wavenumber 60 characteristic of the control because the dissipation occurs over a wider range of wavenumbers). These results might have been anticipated for the following reasons. The strengths of the dissipation in the control and *S*1 runs are fairly similar because of the similarity of the diffusion coefficients noted above. As well, the strength of the dissipation with $S = 1$ is appropriate for a model with resolution T31 and hence is too weak for a T63 simulation. We note from Figs. 3c, 3d and 4 of Frederiksen and Davies (1997) that the net dissipation functions for T15 and T31 resolutions, designed so that they maintain the same large-scale kinetic energy spectra, differ by close to an order of magnitude at their maxima near the largest respective wavenumbers. We might therefore expect that in going from T31 to T63 we would also need to increase the scaling factor *S* by nearly an order of magnitude. This argument is consistent with the results shown in Fig. 6.

The results in Fig. 6 are further examples of the tail-wagging-the-dog effect. This effect is also evident in the different zonal wavenumber spectra $E(m)$ (not shown). For example, as the dissipation strength increases from the control to *S*5, *N*5 and *S*10 the zonal mean kinetic energy increases from $E(0) = 72.6$ to 75. 7, 75. 8 and 77. 4 $m^2\ s^{-2}$. These increases are only moderate but are nevertheless reflected in the mean zonal winds as discussed below.

Next we examine the seasonal dependence of energy spectra for the *S*10 simulation. Fig. 7a shows the mean and mean ± standard deviation of the total wavenumber kinetic energy spectra $e(n)$ for January, April, July and October while Fig. 7b shows the corresponding results for the zonal wavenumber kinetic energy spectra $E(m)$. These results were calculated on the basis of twice daily data for 10 years for each month shown. We note from Figs. 7a and 7b that the $E(m)$ spectra closely follow an $m^{-3}$ spectrum for $m \approx 8$ to 35 in each month while the $e(n)$ spectra are slightly shallower than an $n^{-3}$ spectrum for $n \approx 15$ to 35. The *S*10 run $e(n)$ spectra in fact appear to closely match the observed results of Straus and Ditlevsen (1998). We also note that the main seasonal changes in the spectra occur for the largest scales in the $e(n)$ spectra with the shape and magnitudes at intermediate and small scales of the spectra showing much less change.

### 5.3 Transient kinetic energy cross sections

The improved energy spectra for the *S*10 simulation (and for the *S*5 and *N*5 runs) shown in Figs. 6 and 7 are also reflected in better agreement between simulated and observed transient kinetic energy in physical space. Fig. 8 shows cross sections of zonally averaged transient kinetic energy based on twice daily data for January for 10 years of integration. We note the considerable improvements in the maximum transient kinetic energy in the NH tropospheric jet core, which is now considerably closer to those of the observations (Fig. 4a) compared with the control run results (Fig. 4b). For example, in the NH the peak transient kinetic energy in the *S*10 run is 215 $m^2\ s^{-2}$ compared with 187 $m^2\ s^{-2}$ for the control and 220 $m^2\ s^{-2}$ at 300 mb near 50°N and 231 $m^2\ s^{-2}$ at 250 mb near 40°N in the observations. In the SH the peak transient kinetic energy in the *S*10 run is again improved compared with the control but is still significantly lower than in the observations; the peak values are 167, 144 and 219 $m^2\ s^{-2}$ for the *S*10, control and observations respectively. The S10 simulation used a 15

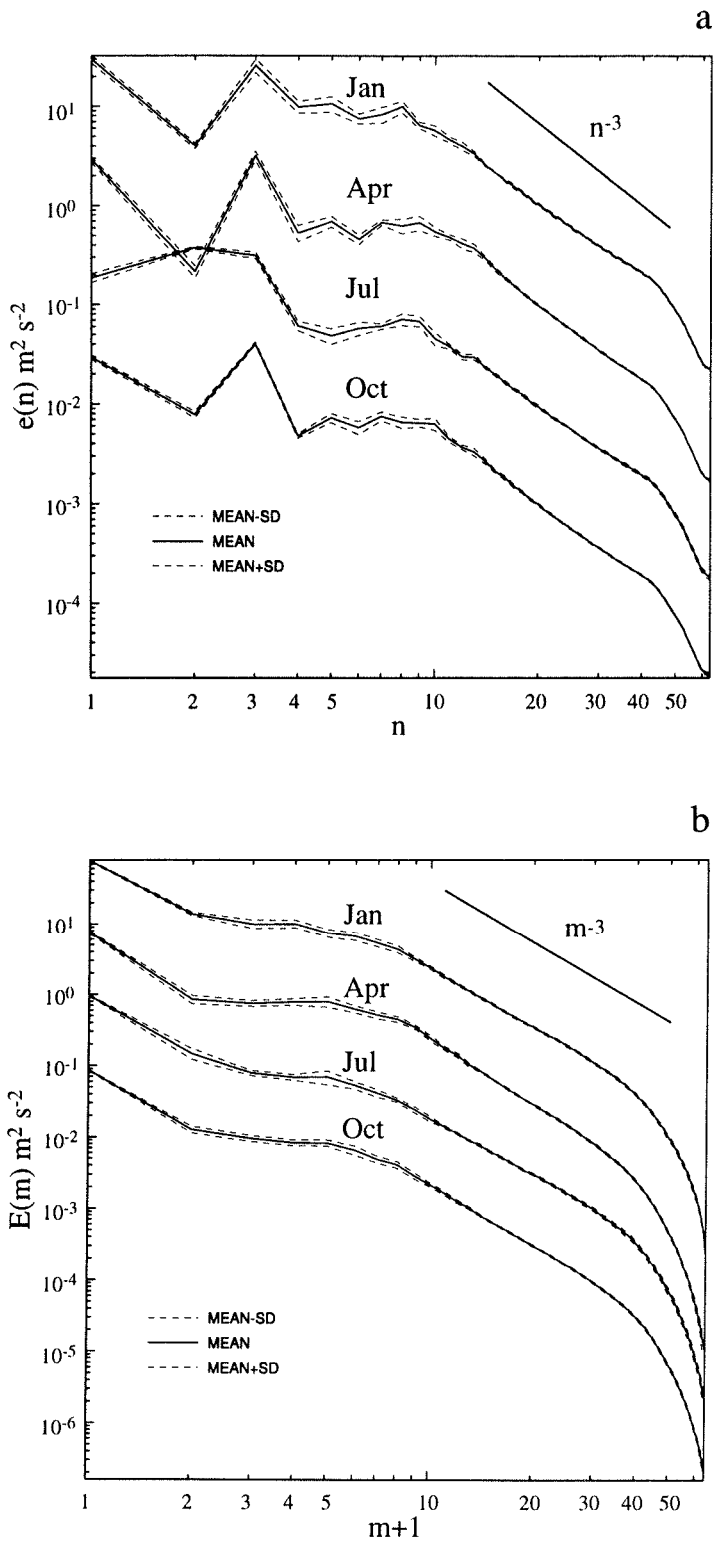


Figure 7 (a) Kinetic energy spectra $e(n)$ $(\mathrm{m^2 s^{-2}})$ (solid) and $e(n) \pm \sigma(n)$ (dashed) for $S10$ simulations.

(b) Kinetic energy spectra $E(m)$ $(\mathrm{m^2 s^{-2}})$ (solid) and $E(m) \pm \Sigma(m)$ (dashed) for $S10$ simulations.

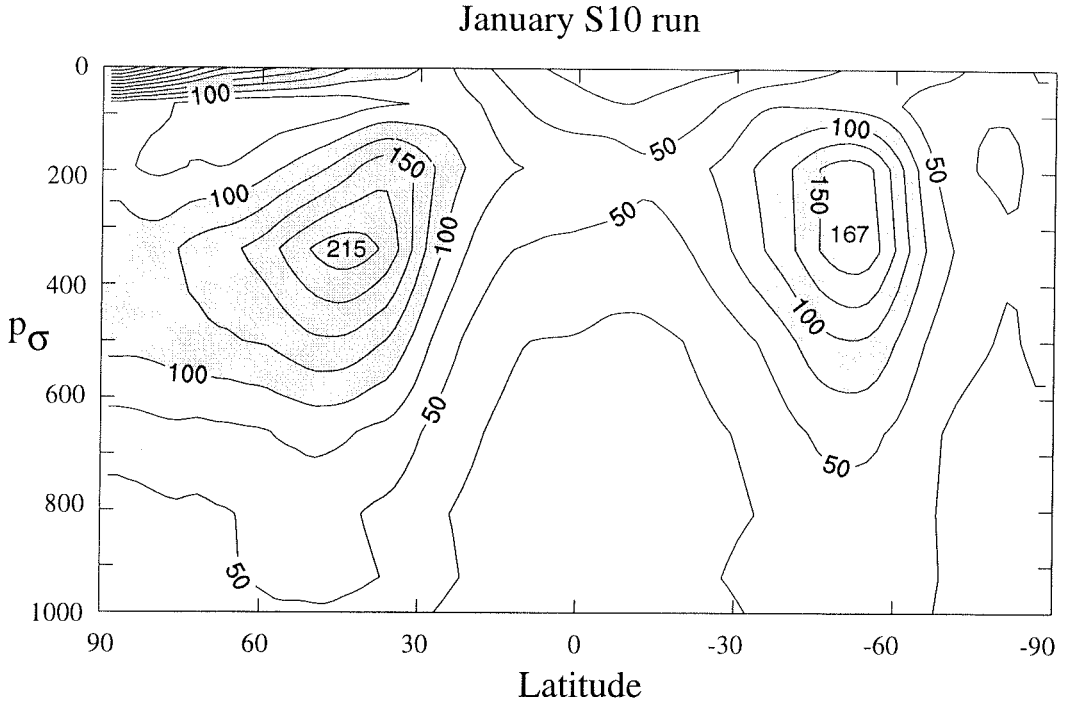


Figure 8 As in Fig.4b for the *S*10 simulation.

minute timestep and unlike the control simulation with this timestep (discussed in section 4) did not result in spurious transients over the southern polar latitudes.

### 5.4 Mean zonal winds

Next, we examine the mean circulations for the *S*5, *N*5 and *S*10 simulations. Fig. 9 shows the mean zonal winds for January, April, July and October as functions of latitude and pressure for the *S*5 run. These results and others presented in this subsection are based on twice daily data taken from 10 years of integrations. Also shown are the differences between the *S*5 results and the control simulation of section 4. Differences that are statistically significant at the 95% confidence level according to Student's t-test are shaded. The t-test is based on 10 monthly averages for each month shown. In general, the differences are statistically significant where their magnitudes are larger than about 1m $s^{-1}$. Fig. 10 shows the corresponding mean zonal winds in the *N*5 simulations. There is a close similarity between the *S*5 and *N*5 results indicating that the mean zonal winds are relatively insensitive to whether the dissipation function $g^{+}(n/n_*)$ or $g(n/n_*)$ is used.

From Fig. 9 we see that in January the net dissipation in the *S*5 run strengthens the NH tropospheric jet by about 2.5 m $s^{-1}$ and moves it slightly equatorward compared with the control mean winds. The SH tropospheric jet is also strengthened by about 4 m $s^{-1}$. In these respects the net eddy dissipation $g^{+}$ improves the simulations over the control. The net dissipation also increases the strength of the easterly stratospheric flow in the tropical and subtropical latitudes; above 100 mb the strength of the flow is largely determined by the

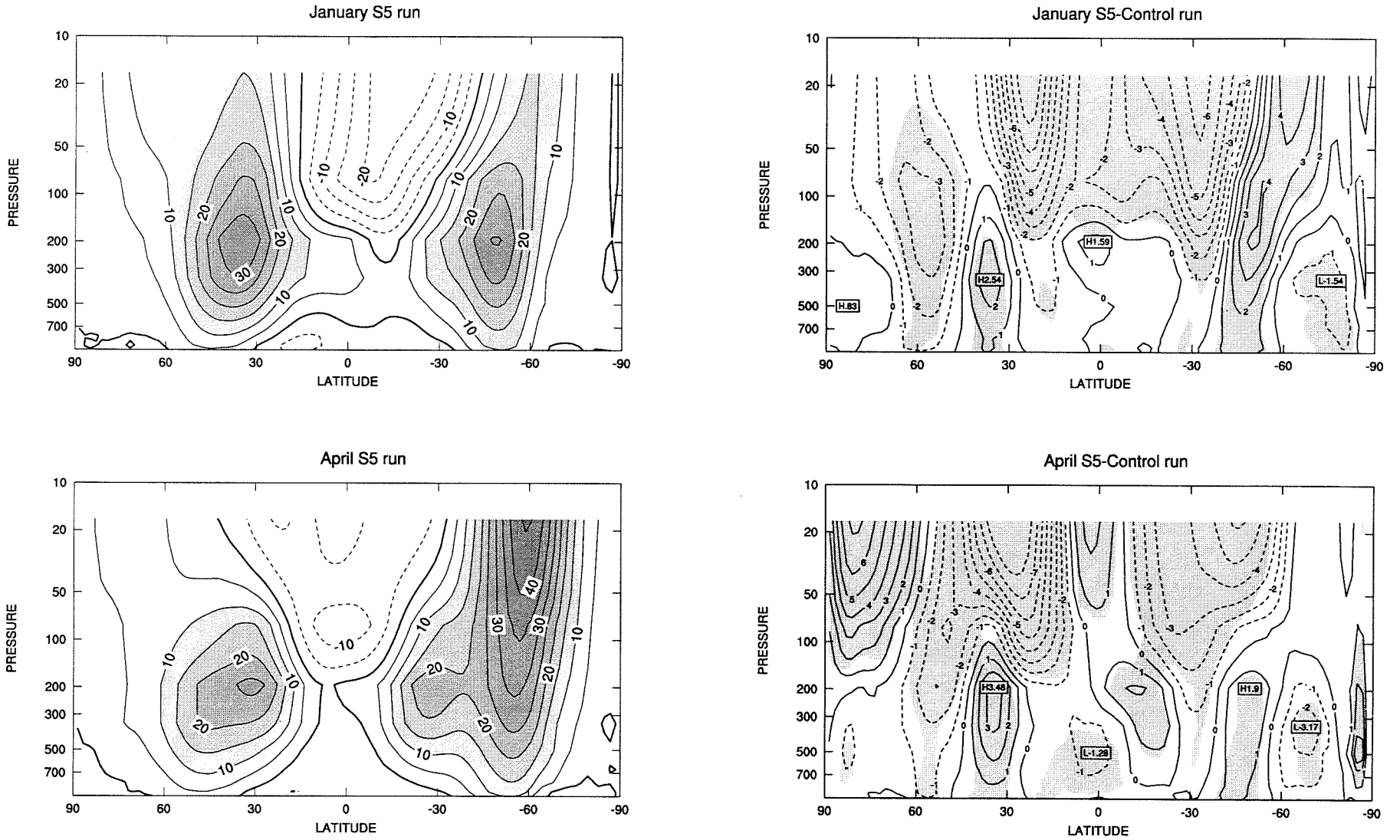


Figure 9 As in Fig.5 for the S5 simulation and differences between S5 and control simulations; on the difference plots results that are statistically significant at the 95% confidence level, according to the Student t-test are shaded.

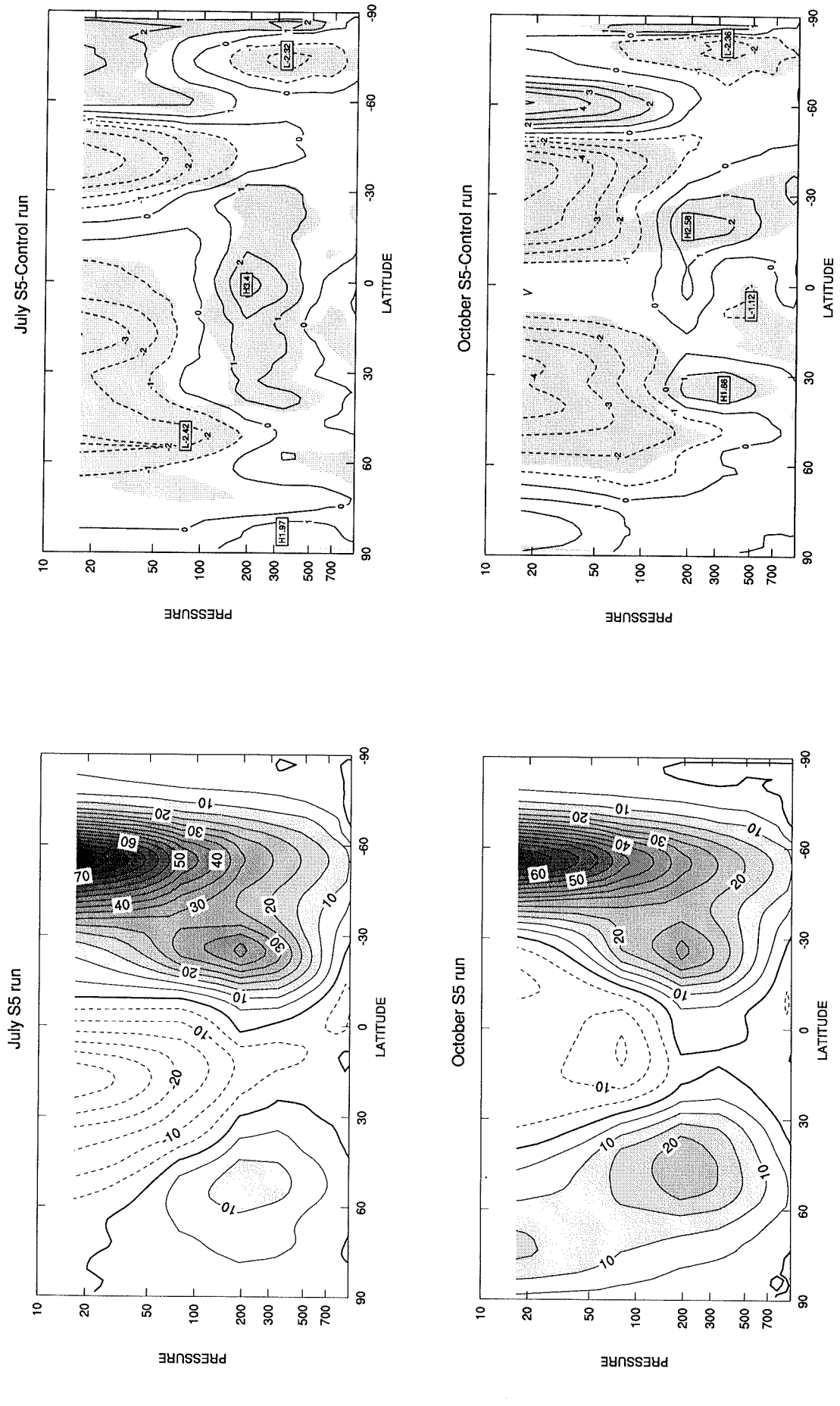


Figure 9 (cont.) As in Fig.5 for the S5 simulation and differences between S5 and control simulations; on the difference plots results that are statistically significant at the 95% confidence level, according to the Student t-test are shaded.

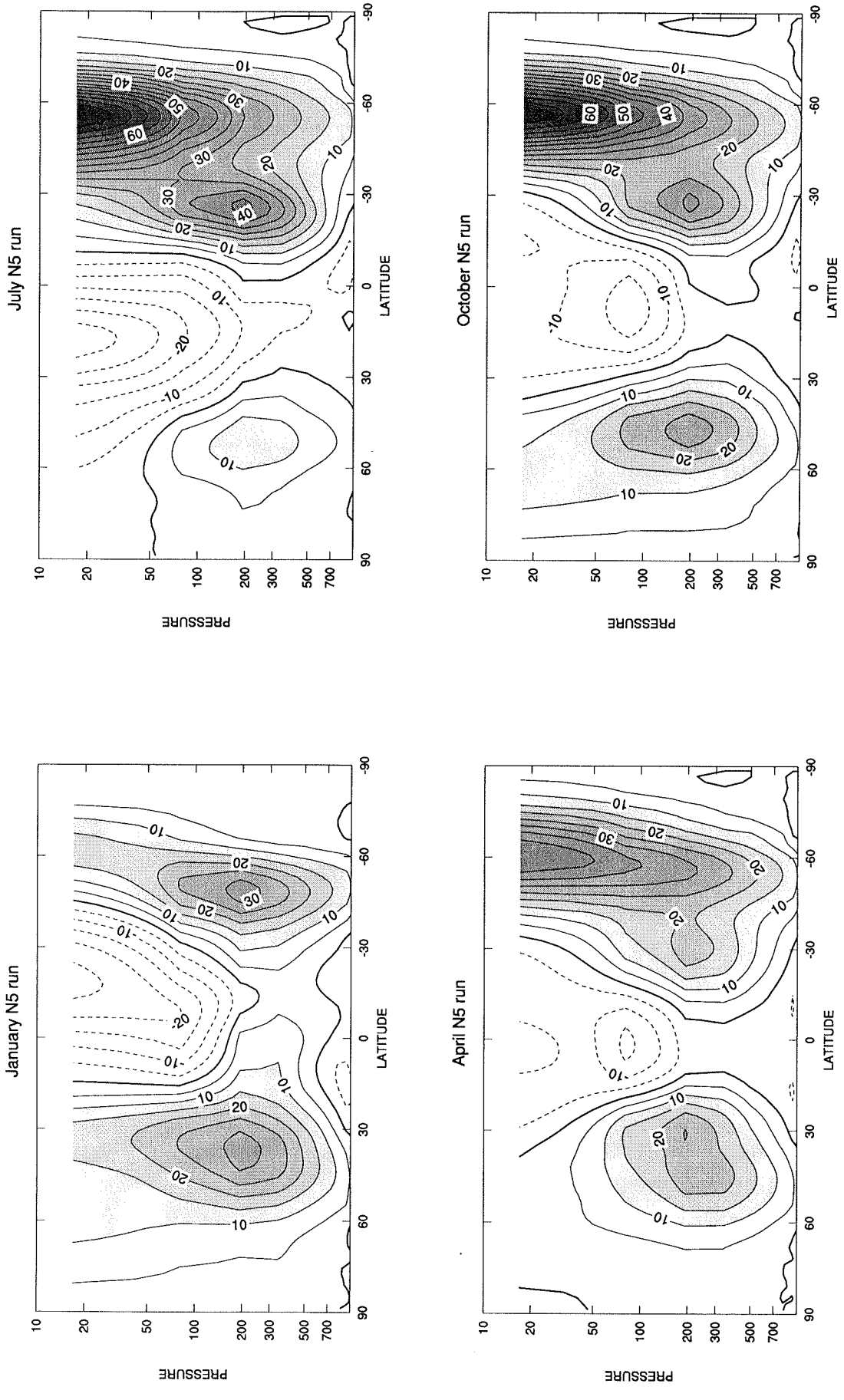


Figure 10 As in Fig.5 for the N5 simulation.

strength of the gravity-wave drag parameterisation used and it may be that increasing its strength would improve the overall simulation. It also seems likely that reducing the strength of the diffusion in the stratosphere would decrease the easterly winds in the tropics and subtropics. This would entail having the strength of the diffusion height dependent and so would be at the expense of an empirical height dependent function. We shall not experiment with such functions here but leave their determination for a subsequent study.

In April, the NH tropospheric jet core for the *S*5 simulations increases in strength by about 3.5 m $s^{-1}$ compared to the control and there is better focussing of the jet maximum near 30 degrees latitude. In these respects the *S*5 runs compare better with the observations. In the SH the improvements in the tropospheric jet strength are less. For the other boreal winter and spring months the improvements in the mean tropospheric winds in the *S*5 runs are similar to those shown for January and April. During boreal summer, particularly in July, there is much less change in the tropospheric extratropics in the *S*5 runs. There is some reduction in the tropospheric easterlies but little change in the too weak NH tropospheric jet. It is clear that there are significant deficiencies in the physical parameterisations, which manifest themselves in the too weak NH jet during boreal summer. The net eddy dissipation parameterisation is not able to compensate for these deficiencies.

In boreal autumn there are again increases in the zonal winds in the tropospheric jet cores in both the NH and SH in the *S*5 run compared with the control run; this is shown in Fig. 9 for October. By December (not shown) there are further increases in the peak values of zonal winds in the troposphere of 3.5 m $s^{-1}$ in the NH and 5.6 m $s^{-1}$ in the SH compared with the control run.

Fig. 11 shows the same fields as in Fig. 9 but for the *S*10 simulations, that is, the mean zonal winds for January, April, July and October and differences between the *S*10 and control runs. The qualitative differences between the *S*10 - control and *S*5 - control results are similar but their magnitudes are generally larger in the *S*10 case involving the stronger diffusion. For example, in January and April the peak zonal winds in the NH tropospheric jet core increase by nearly 5 m $s^{-1}$ compared with the control, giving better comparisons with observations. The SH jet core is also moved equatorward in the *S*10 simulation compared with the control and strengthened by nearly 5 m $s^{-1}$ in boreal winter and nearly 3 m $s^{-1}$ in boreal spring. Again in boreal summer there is little change in the too weak NH tropospheric jet in the *S*10 run compared with the control indicating likely deficiencies in the physical parameterisations described above. There is again an increase in the tropospheric jet maximum in boreal autumn in the *S*10 run as shown for October in Fig. 11 and further increases occur in December of around 3 m $s^{-1}$ in the NH and SH troposphere jet cores.

## 6 Conclusions

We have implemented the net eddy viscosity of Frederiksen and Davies (1997) –FD– as a horizontal diffusion parameterisation within the CSIRO Mark II atmospheric GCM. The form of the FD net eddy viscosity was derived self-consistently from closure theory in such a way that it would maintain the same large-scale kinetic energy spectra in the barotropic vorticity equation with changing resolution. We have examined the ability of the GCM to simulate the annual cycle of zonal winds and transient kinetic energy with the new diffusion

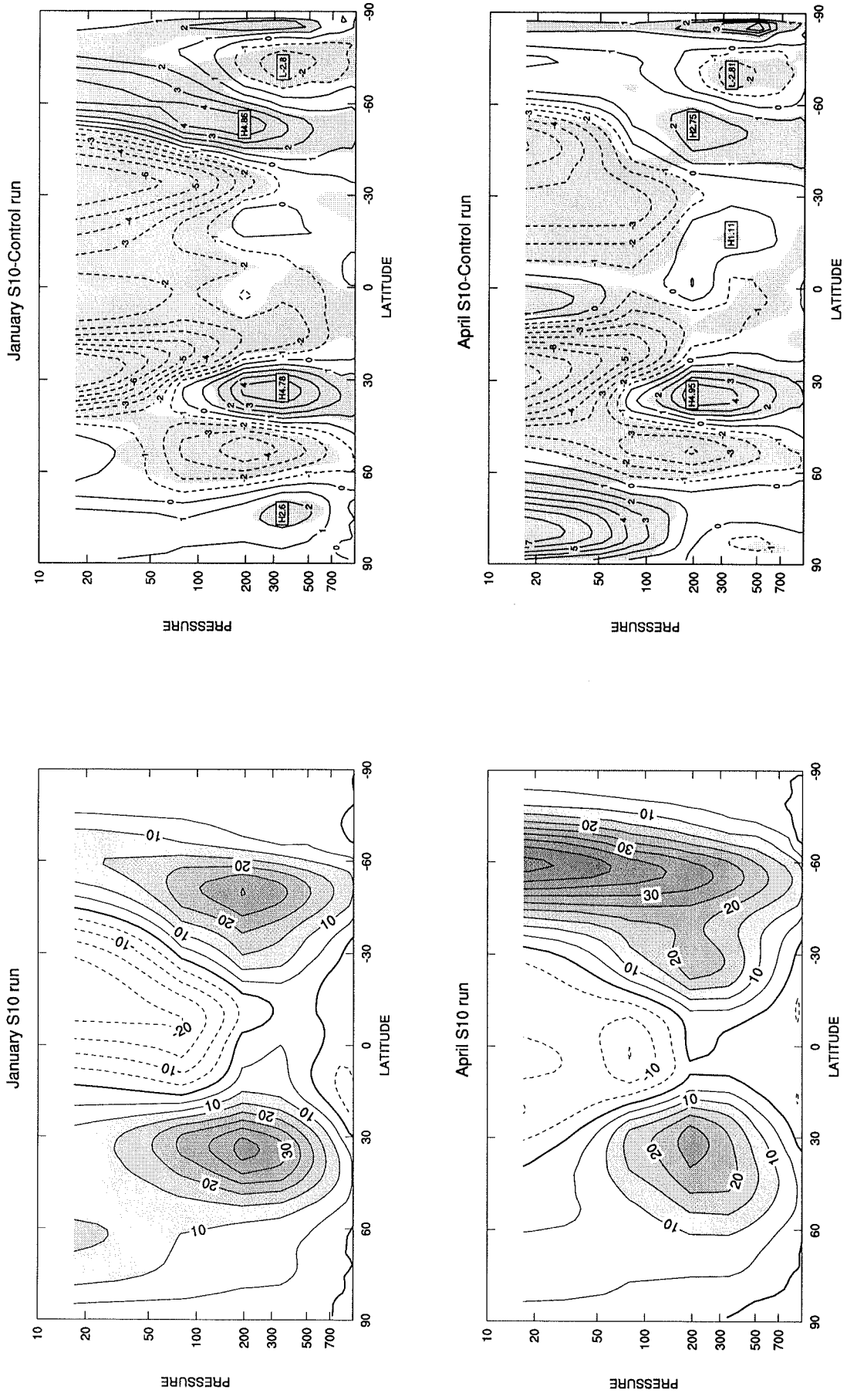


Figure 11 As in Fig.9 for the *S*10 simulation.

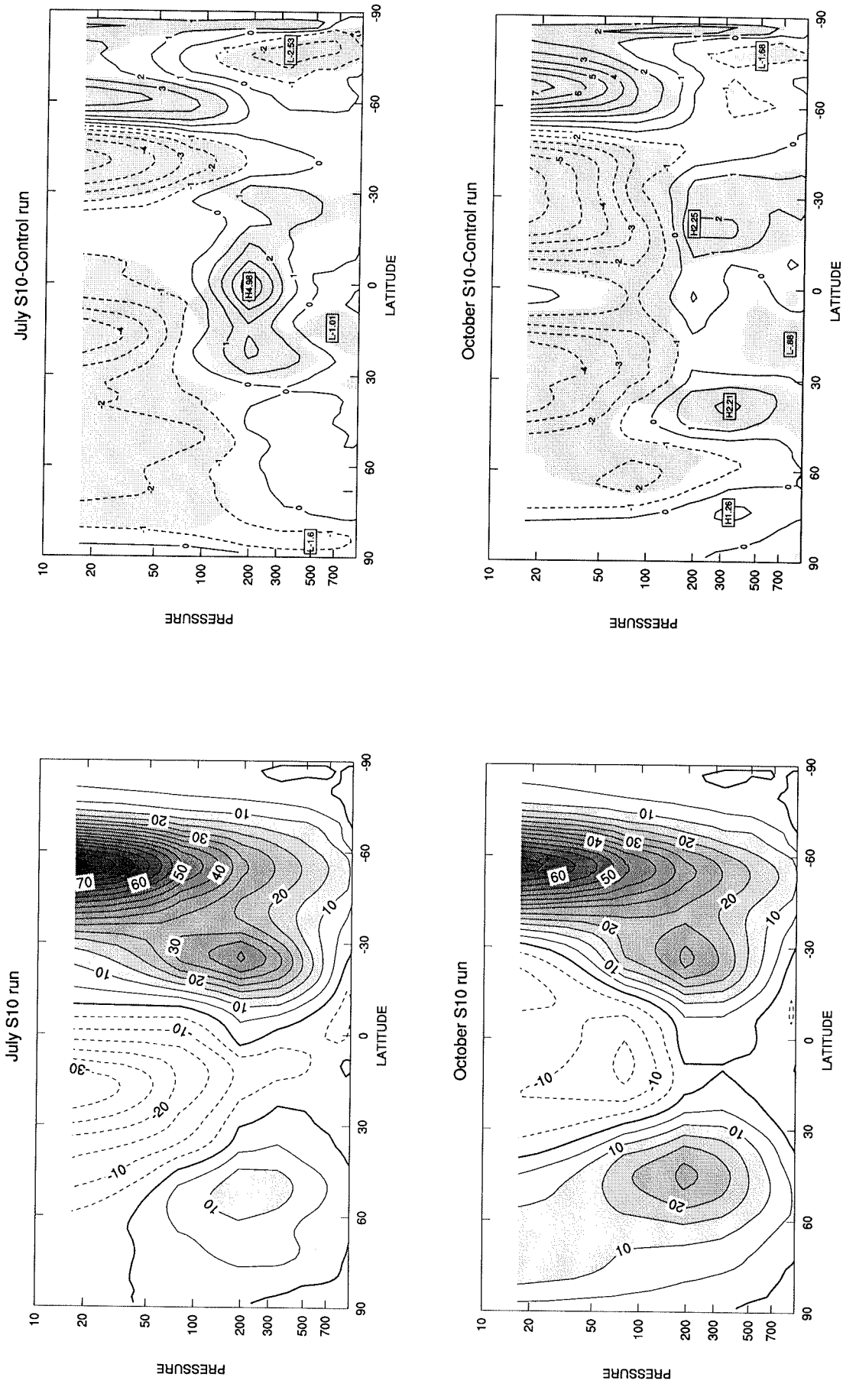


Figure 11 (cont.) As in Fig.9 for the S10 simulation.

parameterisation. We have studied the sensitivity of our results to the choice of diffusion coefficient and focussed on a case, denoted run *S*10, for which we argue the strength of the diffusion is appropriate for simulations at resolution T63. The latitude-pressure cross sections of monthly and zonally averaged zonal winds and transient kinetic energy have been compared with observations and with control simulations using the standard diffusion parameterisation employed in previous studies with this model (e.g. Smith *et al.*, 1998; Smith, 1999 and references therein). We have also compared and contrasted zonal and total wave number spectra of kinetic energy for the FD parameterisation with observations and with control simulations.

The FD parameterisation, particularly for the *S*10 run, has improved the simulations of the CSIRO GCM in a number of ways. Throughout the annual cycle, both the zonal and total wave number spectra now have approximate –3 power laws for a range of intermediate wave numbers, as in the observations (Wiin-Nielsen, 1967, 1972; Boer and Shepherd, 1983; Nastrom *et al.*, 1984), while the control simulation spectra are flatter with zonal wave number spectra following approximate –2 power laws at intermediate scales. In physical space, peak values of transient kinetic energy in the *S*10 run have increased considerably over the control results giving better agreement with the observations. For example, in January monthly and zonally averaged transient kinetic energies are 26 $m^2$ $s^{-2}$ larger near the NH tropospheric jet core and 23 $m^2$ $s^{-2}$ larger near the SH tropospheric jet core in the *S*10 run compared with the control. The *S*10 model is stable with a larger 15 minute timestep while in the control large amplitude spurious transients are generated throughout the atmosphere over the south polar latitudes if the timestep used exceeds four minutes.

The strength and location of the tropospheric jets are also improved with the FD parameterisation in boreal autumn, winter and spring. For the *S*10 run, the monthly and zonally averaged zonal wind in the NH and SH tropospheric jet cores is stronger than in the control by as much as 5 m $s^{-1}$ in boreal winter and spring. In the control simulations the tropospheric jet maxima tend to be located poleward of the observed jets while for the *S*10 run this problem is largely rectified. In boreal summer, the NH tropospheric jet is too weak in both the control and *S*10 simulations indicating that there are significant deficiencies in the thermodynamics of the model which the FD diffusion parameterisation cannot compensate for.

## 7 Acknowledgments

We thank Hal Gordon, John McGregor and Leon Rotstayn for helpful discussions on the structure and specifications of the CSIRO Mark II atmospheric GCM.

## 8 References

Baer, F. and Alyea, F.N., 1971. Effects of spectral truncation on general circulation and long-range prediction. *J. Atmos. Sci.*, **28**, 457-480.

Blackadar, A.K., 1962. The vertical distribution of wind and turbulent exchange in a neutral atmosphere. *J. Geophys. Res.*, **67**, 3095-3102.

Boer, G.J. and Shepherd, T.G., 1983. Large-scale two-dimensional turbulence in the atmosphere. *J. Atmos. Sci.*, **40**, 164-184.

Boer, G.J., McFarlane, N.A., Laprise, R., Henderson, J.D. and Blanchet, J.-P., 1984. The Canadian Climate Centre spectral atmospheric general circulation model. *Atmos.-Ocean*, **22**, 397-429.

Bottomley, M., Folland, C.K., Hsiung, J., Newell, R.E. and Parker, D.E., 1990. Global ocean surface temperature atlas. *U.K. Met. Office*, 20 pp & 313 plates.

Dix, M.R. and Hunt, B.G., 1995. Chaotic influences and the problem of deterministic seasonal predictions. *Int. J. Climatol.*, **15**, 729-752.

Eliasen, E. and Laursen, L., 1990. On the effects of horizontal resolution and diffusion in a two-layer general circulation model with a zonally symmetric forcing. *Tellus*, **42A**, 520-530.

Frederiksen, J.S. and Sawford, B.L., 1980. Statistical dynamics of two-dimensional inviscid flow on a sphere. *J. Atmos. Sci.*, **37**, 717-732.

Frederiksen, J.S. and Davies, A.G., 1997. Eddy viscosity and stochastic backscatter parameterisations on the sphere for atmospheric circulation models. *J. Atmos. Sci.*, **54**, 2475-2492.

Frederiksen, J.S., Dix, M.R. and Kepert, S.M., 1996. Systematic energy errors and the tendency toward canonical equilibrium in atmospheric circulation models. *J. Atmos. Sci.*, **53**, 887-904.

Gordon, H.B. and O'Farrel, S.P., 1997. Transient climate change in the CSIRO coupled model with dynamical sea-ice. *Mon. Wea. Rev.*, **125**, 875-907.

Hollinsworth, A., Cubasch, U., Tibaldi, S., Brankovic, C., Palmer, T.N. and Campbell, L., 1987. Mid-latitude atmospheric prediction on time scales of 10-30 days. *Atmospheric and Oceanic Variability*, H. Cattle, Ed., Royal Meteorological Society, 117-151.

Koshyk, J.N. and Boer, G.J., 1995. Parameterisation of dynamical subgrid-scale processes in a spectral GCM. *J. Atmos. Sci.*, **52**, 965-976.

Kraichnan, R.H., 1967. Inertial ranges in two-dimensional turbulence. *Phys. Fluids*, **10**, 1417-1423.

Kraichnan, R.H., 1971. Inertial-range transfer in two- and three-dimensional turbulence. *J. Fluid* Mech., **47**, 525-535.

Laursen, L. and Eliasen, E., 1989. On the effects of the damping mechanisms in an atmospheric circulation model. *Tellus*, **41A**, 385-400.

Leith, C.E., 1971. Atmospheric predictability and two-dimensional turbulence. *J. Atmos. Sci.*, **28**, 145-161.

Leith, C.E., 1990. Stochastic backscatter in a subgrid-scale model. Plane shear mixing layer. *Phys. Fluids A*, **2**, 297-299.

Manabe, S., Smagorinsky, J. and Stickler, R.F., 1965. Simulated climatology of a general circulation model with a hydrological cycle. *Mon. Wea. Rev.*, **93**, 769-798.

Manabe, S., Smagorinsky, J., Holloway, J.L. and Stone, H.M., 1970. Simulated climatology of a general circulation model with a hydrologic cycle. Part III: Effects of increased horizontal computational resolutions. *Mon. Wea. Rev.*, **98**, 175-212.

Manabe, S., Hahn, D.G. and Holloway Jr., J.L., 1979. *Climate Simulations with GFDL Spectral Models of the Atmosphere: Effect of Spectral Truncation.* GARP Pub. Ser., 22, 41-94.

McGregor, J.L., 1993. Economical determination of departure points for semi-Lagrangian models. *Mon. Wea. Rev.*, **121**, 221-230.

McGregor, J.L., Gordon, H.B., Watterson, I.G., Dix, M.R. and Rotstayn, L.D., 1993. The CSIRO 9-level atmospheric general circulation model. Melbourne, CSIRO Division of Atmospheric Research. (Technical Paper 26), pp.89.

Miyakoda, K., Strickler, R.F., Nappo, C.J., Baker, P.L. and Hembree, G.D., 1971. The effect of horizontal grid resolution in an atmospheric circulation model. *J. Atmos. Sci.*, **28**, 481-499.

Nastrom, G.D. and Gage, K.S., 1985. A climatology of atmospheric wavenumber spectra observed by commercial aircraft. *J. Atmos. Sci.*, **42**, 950-960.

Nastrom, G.D., Gage, K.S. and Jasperson, W.H., 1984. The atmospehric kinetic energy spectrum, $10°$-$10^4$ km. *Nature*, **310**, 36-38.

Piomelli, U., Cabot, W.H., Moin, P. and Lee, S., 1991. Subgrid-scale backscatter in turbulent and transitional flows. *Phys. Fluids A*, **3**, 1766-1771.

Smagorinsky, J., Manabe, S. and Holloway, J.L., 1965. Numerical results from a nine-level general circulation model of the atmosphere. *Mon. Wea. Rev.*, **93**, 727-768.

Smith, I.N., 1999. Estimating mass balance components of the Greenland ice sheet from a long-term GCM simulation. *Global and Planetary Change*, **20**, 19-32.

Smith, I.N., Dix, M. and Allan, R.J., 1997. The effect of greenhouse SSTs on ENSO simulations with an AGCM. *J. Climate*, **10**, 342-352.

Smith, I.N., Budd, W.F. and Reid, P., 1998. Model estimates of Antarctic accumulation rates and their relationship to temperature and changes. *Annals of Glaciol.*, **27**, 246-250.

Straus, D.M. and Ditlevsen, P., 1998. Geophysical turbulence in the reanalyses of ECMWF. Report No. 60 of Center for Ocean-Land-Atmosphere Studies, Calverton, M.D, USA, 50 pp.

Watterson, I.G., Dix, M.R., Gordon, H.B. and McGregor, J.L., 1995. The CSIRO nine-level atmospheric general circulation model and its equilibrium and doubled $CO_2$ climates. *Aust. Meteor. Mag.*, **44**, 111-125.

Watterson, I.G., O'Farrell, S.P. and Dix, M.R., 1997. Energy and water transport in climates simulated by a general circulation model that includes dynamic sea ice. *J. Geophys. Res.*, **102**, 11,027-11,037.

Wiin-Nielsen, A., 1967. On the annual variation and spectral distribution of atmospheric energy. *Tellus*, **19**, 540-559.

Wiin-Nielsen, A., 1972. A study of power laws in the atmospheric kinetic energy spectrum using spherical harmonic functions. *Meteor. Ann.*, **6**, 107-124.